Preparation, geometric structure and magnetism of ultrathin oxide films on metal surfaces

Dissertation

zur Erlangung des

Doktorgrades der Naturwissenschaften (Dr. rer. nat.)

der

Naturwissenschaftlichen Fakultät II

Chemie und Physik

der Martin-Luther-Universität

Halle-Wittenberg,

vorgelegt

von Herr Dipl.-Phys. Florian Klimenta

geb. am 17.12.1982 in Halberstadt

Halle (Saale), 28.09.2012

Danksagungen

Ich bedanke mich bei

Herrn Professor J. Kirschner für die Möglichkeit, meine Dissertation am Max-Planck-Institut für Mikrostrukturphysik in Halle anzufertigen,

PD Dr. H. L. Meyerheim für die ausführliche Betreuung und die ausserordentlich schnelle Beantwortung jedweder Fragen,

Herrn F. Weiß für die technische Unterstützung und die produktiven Gespräche,

Frau H. Menge für die schnelle und gewissenhafte Abhandlung aller kristallbezogener Anliegen,

Dr. R. Bali für die unzähligen wissenschaftlichen Diskussionen

sowie allen weiteren Mitarbeiterinnen und Mitarbeitern des Max-Planck-Instituts für eine angenehme und produktive Atmosphäre.

Abstract

Controlling magnetism with electric fields is a topic on which a lot of research activity has been spent with one of the possible goals being the realization of a functional four state memory[1]. Here the magnetoresitance of a Magnetic Tunneling Junction (MTJ) is not only influenced by the parallel or antiparallel alignment of the ferromagnetic material but also by the polarization of the ferroelectric barrier.[2] The straightforward solution to the combination of these two effects would be to use materials combining both ferroelectricity and ferromagnetism, so called multiferroics[3] but since they are few and far between[4] it seems more promising to utilize multiferroic interfaces between ferroelectric and ferromagnetic components.[5–8] Garcia et al.[9] have proven that the $BaTiO_3$/Fe interface can be used to exert control over magnetism and spin polarization through the interfacial mutiferroic coupling. Thus this system is a very interesting object of research to characterize its properties.

This work focusses on structural investigations using in-situ Surface X-Ray Diffraction on $BaTiO_3$ films grown on Fe(001) single crystals. The films were pre-characterized using Low Energy Electron Diffraction, Auger Electron Spectroscopy and Scanning Tunneling Microscopy to confirm ordered growth. This is supported by theoretical calculations relating to the film stability and its magnetic properties and is expanded to additional metallic samples, namely Pd(001) and Pt(001). Gaining knowledge about the ferroelectric/ferromagnetic interface is only part of the information necessary to realize an MTJ utilized by Garcia et al.[9] and thus the system has to be flipped by growing metal on the $BaTiO_3$. Growing Iron on Barium Titanate thin films and single crystals is performed to acquire this information.

The preparation of $BaTiO_3$ crystals leads to another interesting question about the structure of the $BaTiO_3$(001)-(2 × 1) reconstruction found on the single crystals used as a substrate for the Fe growth. This question is answered in the last part of this work providing a model for the Perovskite surface not considered so far.

Zusammenfassung

Magnetismus mit Hilfe von elektrischen Feldern zu kontrollieren ist schon länger ein wichtiges Forschungsgebiet welches zum Beispiel zu der Realisierung von Vier-Zustands-Speichern[1] für die Computerindustrie führen soll. Hierbei wird der Magnetwiderstand von magnetischen Tunnelkontakten (MTJ) nicht nur durch die parallele und antiparallele Ausrichtung der ferromagnetischen Materialien, sondern auch durch die Polarisierung der ferroelektrischen Barriere beeinflusst.[2] Was liegt da näher, als ein Material zu verwenden, das beide Eigenschaften in sich vereint: Multiferroika?[3] Jedoch sind diese Materialen sehr selten zu finden und schwer herzustellen,[4] daher ist es viel erfolgversprechender multiferroische Grenzflächen zu erzeugen indem man ferroelektrische und ferromagnetische Materialien verbindet.[5–8] Garcia *et al.*[9] haben bewiesen, dass die $BaTiO_3$/Fe Grenzfläche verwendet werden kann um Magnetismus und Spinpolarization durch multiferroische Wechselwirkung an der Grenzfläche zu beeinflussen. Daher ist dieses System ein sehr interessantes Forschungsobjekt um dessen Eigenschaften zu ergründen.

Diese Arbeit konzentriert sich darauf, die geometrische Struktur von $BaTiO_3$ Filmen gewachsen auf Fe(001)-Einkristallen mittels Oberflächenröntgenbeugung (SXRD) zu untersuchen. Zu diesem Zweck wurden die Schichten zusätzlich mittels Beugung niederenergetischer Elektronen, Augerelektronen-Spektroskopie und Rastertunnelmikroskopie (LEED, AES und STM) charakterisiert. Dies wird weiterhin durch theoretische Berechnungen unterstützt, welche sich mit der Stabilität des Films und dessen magnetischen Eigenschaften befassen, und erweitert durch das Einbeziehen von Pd(001) und Pt(001) als Substratkristalle. Wissen über die ferroelektrisch/ferromagnetische Grenzfläche ist nur ein Teil der benötigten Informationen um einen magnetischen Tunnelkontakt wie den von Garcia *et al.*[9] zu realisieren. Zusätzlich benötigt wird Wissen über das Wachstum des Ferromagnetika auf der ferroelektrischen Barriere. Der Versuch, Eisen auf Bariumtitanatfilmen und -einkristallen zu wachsen soll dieses Wissen liefern.

Die Präparation von $BaTiO_3$ Kristallen führt zu einer weiteren interessanten Frage nach der geometrischen Struktur der $BaTiO_3$(001)-(2×1)-Rekonstruktion, welche sich auf den Einkristallen nach der Präparation ergibt. Diese Frage wird im letzten Teil dieser Arbeit beantwortet durch die Entwicklung eines Modells

für diese Perovskitoberfläche, welches bisher noch nicht in Betracht gezogen wurde.

Contents

i

List of Figures

List of Acronyms

AES   Auger Electron Spectroscopy

BTO   Barium Titanate

CMA   Cylindrical Mirror Analyzer

CTR   Crystal Truncation Rod

DOS   Density of States

ESRF   European Synchrotron Radiation Facility

IBAD   Ion Beam Assisted Deposition

LASER   Light Amplification through Stimulated Emission of Radiation

LEED   Low Energy Electron Diffraction

MBE   Molecular Beam Epitaxy

MTJ   Magnetic Tunneling Junction

PLD   Pulsed Laser Deposition

SLR   Superlattice Rod

STM   Scanning Tunneling Microscopy

SXRD   Surface X-Ray Diffraction

TE   Thermal Evaporation

UHV   Ultra-High Vacuum

VASP   Vienna Ab-initio Simulation Package

Chapter 1

Theoretical Basics and Experimental Procedures

Every experiment starts with at least a basic understanding of the theoretical foundation. This chapter gives a short overview of the material in question (Barium Titanate), followed by an introduction into the used methods for growing and investigating the sample. It will conclude with a more comprehensive section about Surface X-Ray Diffraction, which is the main method of investigation in this work. The information presented in this chapter is based on a few primary sources like *Solid Surfaces, Interfaces and Thin Films* by H. Lüth[10] for the baseline information of most of the used investigative methods. More in depth information has been gathered from *Pulsed Laser Deposition of Thin Films* by R. Eason[11] or *Scanning tunneling microscopy - from birth to adolescence* by G. Binnig and H. Rohrer[12] for the sections on the respective topics (1.2.2 and 1.3.3). Big parts of section 1.3.4 are based on the works by Feidenhans'l[13] and Robinson[14, 15]. If not otherwise stated, all structural parameters used in this work which have not been calculated in the analysis process were taken from *Landolt-Börnstein III/36A1*[16] or directly calculated from these.

1.1 Barium Titanate (BTO)

Barium Titanate is a ternary oxide crystallizing in the well known perovskite structure as shown in Figure 1.1. Here the Titanium (small blue sphere) sits
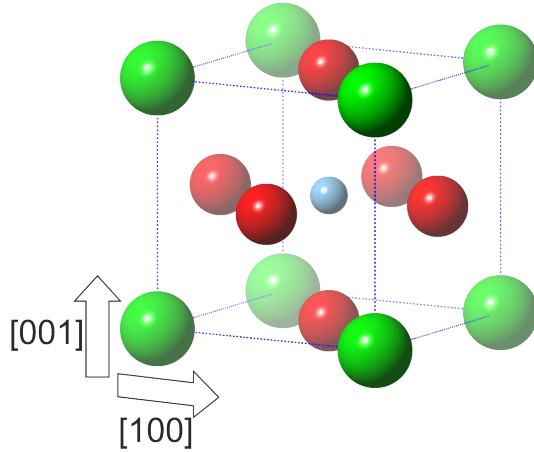
Figure 1.1: Unit cell of the BaTiO$_3$ crystal with Barium, Titanium and Oxygen represented as big green, small blue and red spheres, respectively.

inside an Oxygen octahedron (red spheres) whose atoms are located at the face centers of the Barium cube (big green spheres). The shown structure is the paraelectric cubic phase of BaTiO$_3$ existing above 396 K which transforms into the ferroelectric tetragonal phase below that temperature. The tetragonal phase is defined by an elongation in one of the $\langle 100 \rangle$ directions and a shift of the Ti- and O-atoms with opposite signs along this direction (Figure 1.2(b)). This leads to a vertical shift between anion and cation where the Oxygen atom is always below (or above, depending on the viewing direction) the other atom of its plane (BaO or TiO$_2$). Further decreasing the temperature will lead to an orthorombic phase below 278 K and a rhombohedral phase below 183 K. In these phases the direction of elongation successively changes from $\langle 100 \rangle$ to $\langle 110 \rangle$ (orthorombic) and $\langle 111 \rangle$ (rhombohedral).

The vertical shift of the Titanium out of the Oxygen plane in the tetragonal phase can reach a bulk value of 0.11 Å[16], creating an electric dipole and with it a spontaneous polarization of BaTiO$_3$[4, 17–20]. In addition to being temperature dependent (vanishing polarization at curie temperature of 396 K) the polarization is also dependent on the lattice deformation. Figure 1.3 shows the results of theoretical calculations performed at the Max Planck Institute of Microstructure Physics, Halle(Saale) (Germany)[21] in which the Titanium shift is represented by long (d_L) and short (d_S) Ti-O bonds between the Titanium and adjacent BaO-layer Oxygen. The diagram displays the changes in these bond lengths relative to the change of the lattice constant c normal to
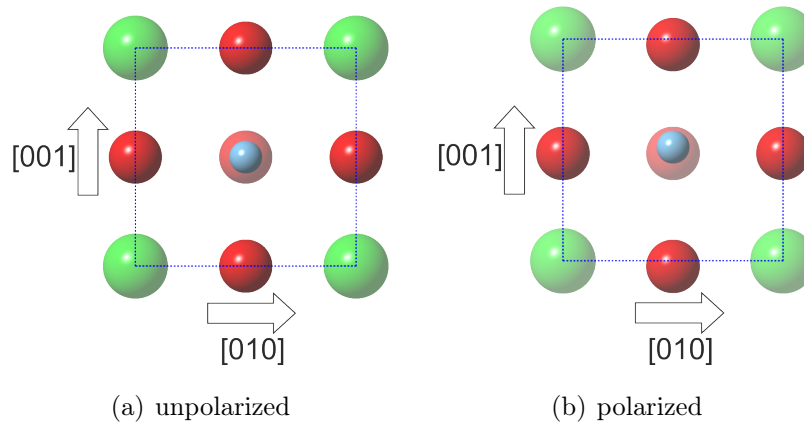
Figure 1.2: Comparison of the unpolarized and polarized unit cell of a bulk $BaTiO_3$ crystal

the sample surface for the case of a bulklike $\frac{c}{a}$-ratio (blue), a smaller $\frac{c}{a}$-ratio closer to the cubic phase (black) and a variable ratio with a constant volume of the unit cell (red). The calculations show an increasing Titanium shift with increasing c which is only weakly influenced by the $\frac{c}{a}$-ratio in such a way that an increasing $\frac{c}{a}$ slightly decreases the vertical shift. Furthermore, a point exists in the diagram where the Titanium resides in the center of the Oxygen octahedron and the polarization vanishes. This happens at about 3% compression in c direction relative to the bulk value which is in good agreement with the 3.5% calculated by Miyazawa *et al.*[20]

The starting models for the investigations in this work are based on the tetragonal phase with lattice parameters of $a = b = 3.9920\,\text{Å}$ and $c = 4.0361\,\text{Å}$ at 20°C with the in-plane parameters being adjusted for the lattice mismatch between $BaTiO_3$ and the substrate in the case of thin film Barium Titanate. Because the cubic phase will be present during heating of the bulk crystal its lattice parameter will also be noted: $a = 3.996\,\text{Å}$ at 120°C. With increasing temperature these lattice parameters will increase inside the tetragonal phase and there is a strong decrease of cell volume when going to the cubic phase after which the lattice parameters will again increase with temperature. The decrease can be neglected during preparation of ultra thin layers, less so in the bulk regime where it can lead to fracturing of the single crystal.
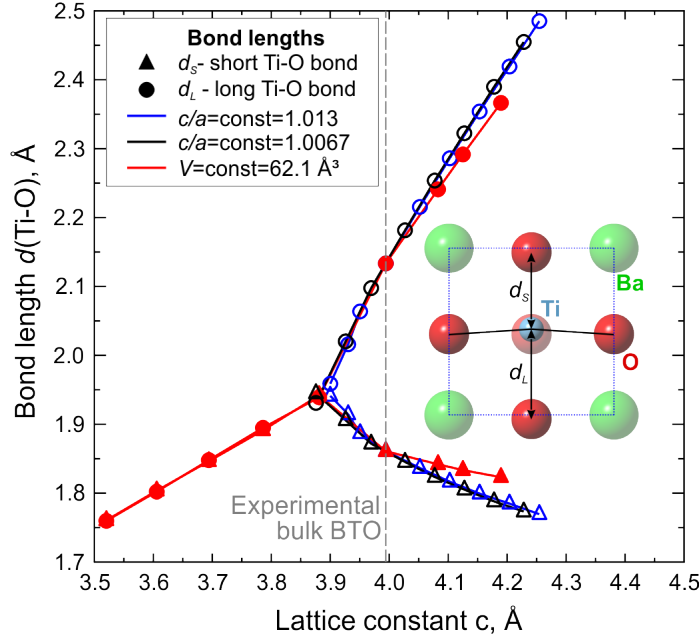
Figure 1.3: Vertical Ti-O bond lengths calculated for different lattice constants and c/a ratios for $BaTiO_3$.[22]

1.2 Growing the film

When investigating a thin film it is important to not only know about the deposited material, but also about the growth itself. In this work Pulsed Laser Deposition and Thermal Evaporation have been applied to grow the thin films. After adressing the possible modes of thin film growth these methods will be introduced.

1.2.1 Three modes of growth

When a particle impinges on a surface it can either leave it via evaporation or diffuse along the surface, depending on the energy of that particle. If then this diffusion does not lead to a delayed re-evaporation it will lead to adsorption at special defect sites (such as ledges or kinks) or nucleation of multiple particles to an island of film material. Further addition of impinging particles to either the defect sites or the island advances the film growth. As seen in Figure 1.4, also interdiffusion has to be considered when modelling the interface of film and substrate.

In order to describe the film growth a set of three markedly different modes
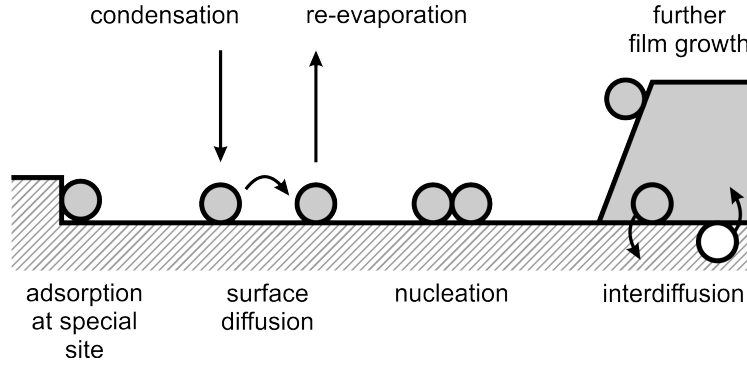
Figure 1.4: Atomic processes during film growth with film atoms as grey circles and a substrate atom in white. Substrate and film are shown as shaded and fully grey areas, respectively.[10]

have been described (Figure 1.5). The first is known as Frank-van der Merve growth in which the film grows in an ordered layer-by-layer fashion. Here the interaction between the substrate and film atoms and the interaction between the atoms inside one layer is stronger than the interaction between the different film layers. In this case a new layer starts growing only when the preceding layer is completely finished. Vollmer-Weber growth is exactly the opposite case, where the interaction between the film atoms is stronger than the interaction between the film and substrate atoms. This leads to island growth in which the islands extend over multiple layers of film material without fully covering the substrate. As an intermediate case the Stranski-Krastanov growth describes a mode where the film starts with a layer-by-layer growth, forming one or more closed layers, and then continues with growing islands on top of these layers.

When looking at the specific surface or interface energy γ necessary to create additional surface, one can express the force equilibrium at a point where substrate and island touch as:

$$\gamma_S = \gamma_{\frac{S}{F}} + \gamma_F \cos \Theta \tag{1.1}$$

where γ_S, γ_F and $\gamma_{\frac{S}{F}}$ are the surface free energy of the substrate-vacuum, the film-vacuum and the substrate-film interface, respectively. Θ, the angle between the substrate and film normal, can be used to distinguish the two extremes of layer-by-layer and island growth:

$$(i) layer : \Theta = 0, \ \gamma_S \geq \gamma_F + \gamma_{\frac{S}{F}} \tag{1.2a}$$

$$(ii) island : \Theta > 0, \ \gamma_S < \gamma_F + \gamma_{\frac{S}{F}} \tag{1.2b}$$

(a) island growth   (b) layer-by-layer growth   (c) layer-then-island growth
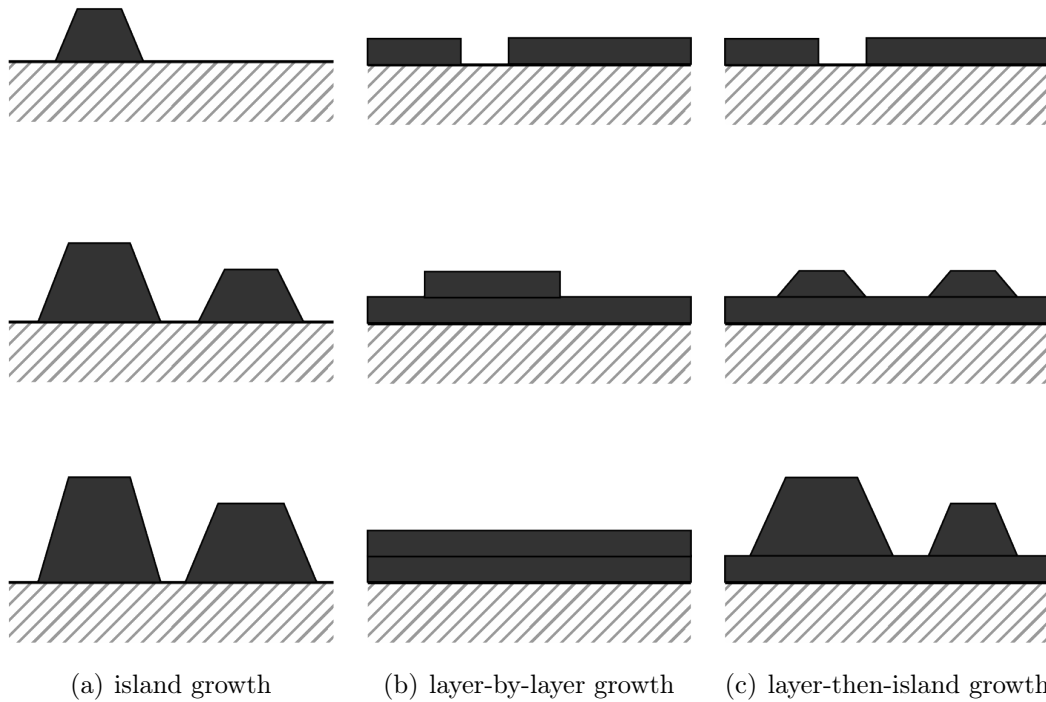
Figure 1.5: Schematic view of the primary modes of thin film growth with increasing thickness from top to bottom (less than one layer, between one and two layers and two layers or more, respectively). (a)Vollmer-Weber mode is pure island growth, (b)Frank-van der Merwe is layer-by-layer growth and (c)Stranski-Krastanov is a combination where the film grows as a closed layer first and then continues with island growth.[10]

This picture can easily explain the Stranski-Krastanov growth mode with the inclusion of a lattice mismatch between substrate and film. The film lattice tries to adjust to the substrate lattice at the cost of deformation energy and the transition from layer-by-layer to island growth marks the point when the elastic strain field exceeds the range of the adhesion forces within the deposited material. The simplification necessary to justify this model is the absence of a vapor phase.

1.2.2   Pulsed Laser Deposition (PLD)

Pulsed Laser Deposition is a vacuum system deposition process commonly used for the growth of complex compounds' thin films with the first reported deposition by Smith and Turner in 1965.[23] Main advantages of this method

are stoichiometric deposition and an easily controllable fluence with a high maximum rate.
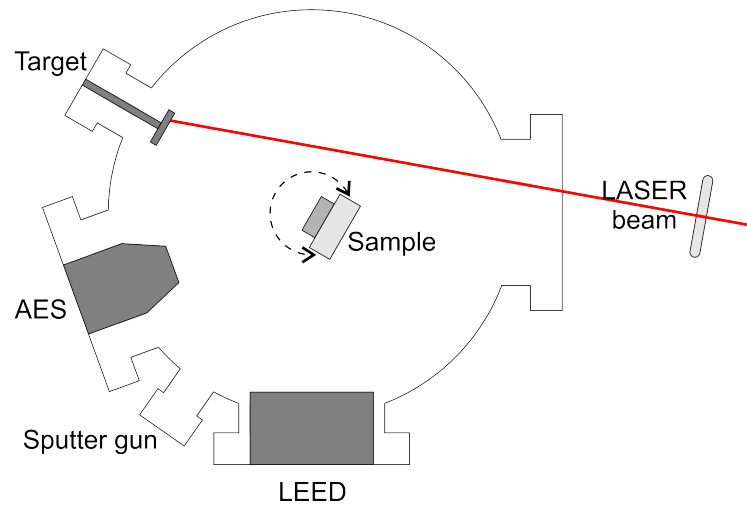
Figure 1.6: Schematic of the main preparation and investigation chamber for this work. Included is the relative position of the sample and rotating target with an indication of the LASER beam in red. Also included are the positions of the AES, LEED and sputter gun (sizes not representative).
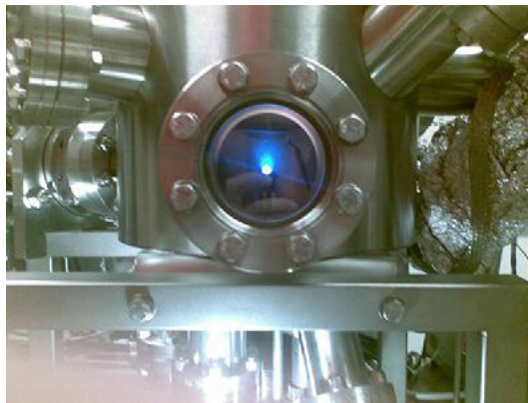
Figure 1.7: Image of a PLD plasma plume

Figure 1.6 shows a schematic view of a PLD setup, where the LASER beam coming from the right enters the UHV chamber and is focused on a rotating target. Here the target material is ablated either through heating or by vaporizing areas of the target surface, depending on the LASER fluence and absorption capabilities of the target material. For PLD it is favorable to choose the fluence and wavelength of the LASER in such a way, that the target is locally vaporized independent of the vapor pressures of the constituents, creating

a plasma plume as seen in Figure 1.7. This is necessary to deposit a film with the same stoichiometry as the target material, which becomes impossible for thermal evaporation of materials consiting of atoms with large differences in the vapor pressure. The high fluence of the LASER thus allows the deposition of the exact target composition onto the sample, with the exception that for oxides the deposition is usually carried out in an oxygen atmosphere with pressures up to 0.1 mbar to achieve the correct oxygen content. High fluence also means a high deposition rate and the fluence necessary to deposit independent of the vapor pressures defines a minimum for this rate. For even smaller deposition rates one can decrease the repetition rate of the LASER or increase the distance between sample and target.

Negative aspects of the high-fluence evaporation of the target are the possible formation of droplets or larger clusters which can hamper the formation of high quality thin films and also the high kinetic energy of the ablated material (some 100 eV[24] possible) can result in implantation of the film material into the sample bulk. The amount of droplets und clusters have been proven to decrease by using high pressure pressed targets or even single crystals if possible. The kinetic energy can be decreased by increasing the base pressure and thus decreasing the mean free path of the atoms in the plasma plume.

1.2.3 Thermal Evaporation

As second deposition method Thermal Evaporation is used, which has been established as the main method for performing Molecular Beam Epitaxy and is also used to lower the pressure in a UHV chamber via sublimation pumps. There are many different evaporation sources available and two have been used in the present work. The first one, used for deposition of Titanium, is an in-house Ion Beam Assisted Deposition (IBAD) source (shown in Figure 1.8) which is similar in operation to the commercially available EFM3 source by Omicron NanoTechnology GmbH[25]. In this source a metallic rod is heated by a tungsten ring filament with typical voltages of $500 - 1500$ V between cathode and anode and when the temperature of the rod is high enough evaporation starts and the atoms leave the source in the direction of the sample. Here the atoms impinge on the surface and the formation of a film may start.[26]

Another method of evaporation is employed by the use of Barium Flash
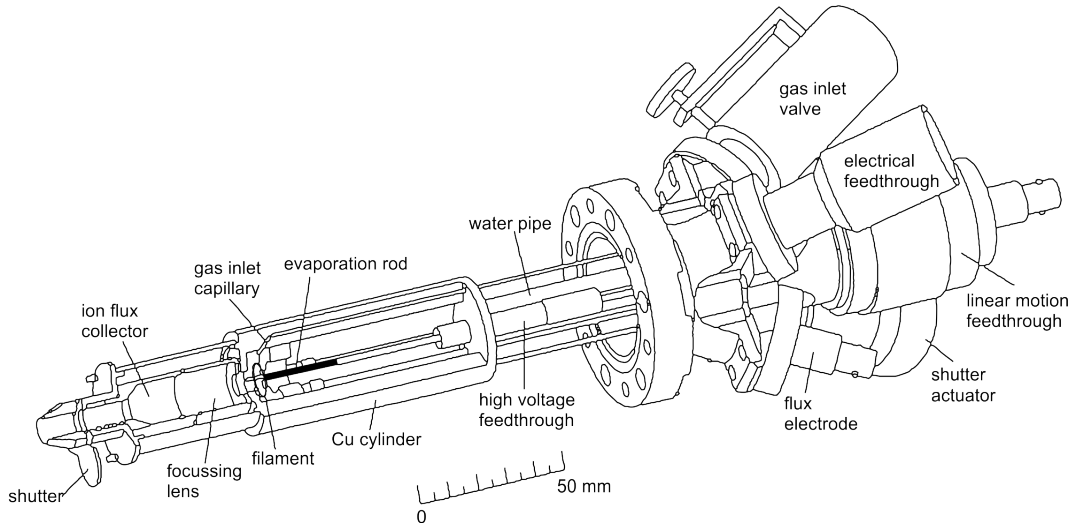
Figure 1.8: IBAD evaporator for thermal deposition of metals.[26]

Getters comercially available from Saes Getters S.p.A. These consist of a crucible filled with a mixture of powdered Barium-Aluminum alloy and powdered Nickel. When this mixture is heated to 800°C Aluminum and Nickel react exothermically and Barium is forced to evaporate. With this method pure Barium is usually deposited inside cathode ray tubes, but it can easily be used to create a film of Barium on a substrate.[27]

1.3   Investigating the quality and structure of the film

After deposition the structure quality has to be checked before the time consuming process of a full structure analysis is performed on an inferior film. The first task is checking the thickness and composition of the film with Auger Electron Spectroscopy followed by an analysis of the order quality and type of reconstruction with Low Energy Electron Diffraction. After the film quality has been deemed good the in-depth structure analysis is performed by measuring the reciprocal space with Surface X-Ray Diffraction and analyzing the measured data.

1.3.1 Auger Electron Spectroscopy (AES)

Auger Electron Spectroscopy is a method for checking the composition of a film and detecting contaminations on surfaces which is easily implemented and fast to perform. It is based on the emission of element specific Auger electrons. This occurs when an electron in an inner shell of the atom is excited by another electron or photon in such a way that it leaves the atom. Now a vacancy is formed which is rapidly filled by an electron from a higher shell which relaxes by either emitting an X-Ray photon or by radiationless emission of another electron of the same or higher shell called the Auger electron (Figure 1.9).
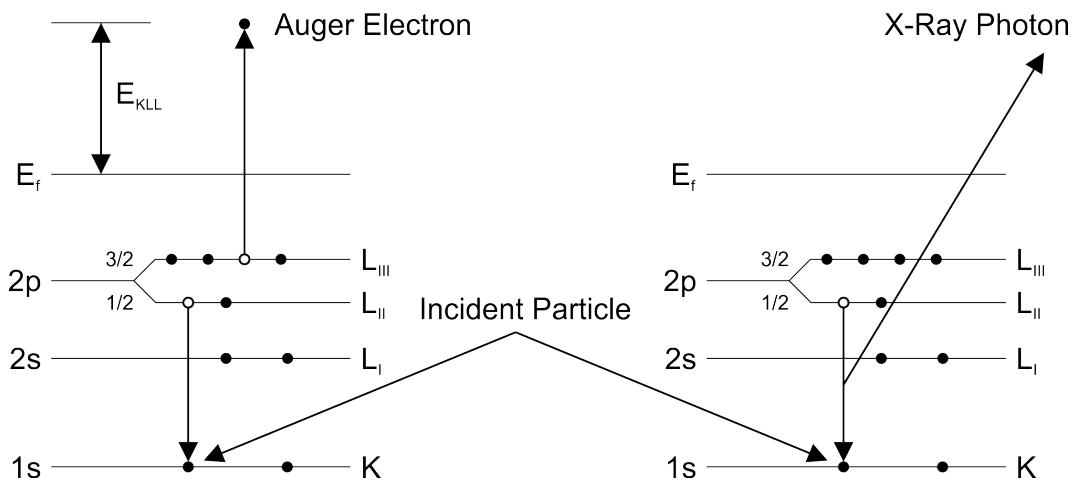
Figure 1.9: Schematic diagram of Auger Electron Spectroscopy (left) and X-Ray fluorescence (right). The incident particle causes the ejection of a K shell electron.[28]

The emitted Auger electron has a well defined element specific energy defined by the difference in energy between the core level vacancy and the electron filling the gap minus the energy necessary to emit the Auger electron. Measuring this energy can identify the corresponding chemical element with a sensitivity of up to 10^{-3} monolayers and a maximum penetration of $10 - 30\,\text{Å}$ because of the limited escape depth of electrons. Since inelastically scattered electrons create a large background the measured signal is usually differentiated to improve the visibility of the weak signal. This can be done without loss of data unless one needs to investigate the line shape and energy shifts due to different chemical surroundings.

AES is usually performed by using an electron gun to create the excitation of the sample atoms and a Cylindrical Mirror Analyzer (CMA) to measure the

energy of the Auger electrons. Figure 1.10 shows a schematic view of half of such an analyzer. Electrons passing the entrance windows of the analyzer are focused onto the channeltron by two concentric cylinders which act as an energy filter (Figure 1.10(a)). Changing the electric field between the cylinders enables the system to scan the chosen range in elecron energies and the channeltron detects the corresponding electron beam intensities. A common problem with this method is sample misalignment. The effect of sample misalignment in z direction is shown in Figure 1.10(b). The measured energies E_M in this case are shifted relative to the Auger electron energy E_A by a static offset which can be used to correctly align the sample or recalculate the data when a reference peak in the spectrum can be identified.

(a) Sensitivity to energy of electrons

(b) Sensitivity to position of the sample

Figure 1.10: Schematic diagram of the upper half of a cross section of a Cylindrical Mirror Analyzer. The upper diagram illustrates the energy selectivity of the analyzer, and the bottom illustrates the importance of alignin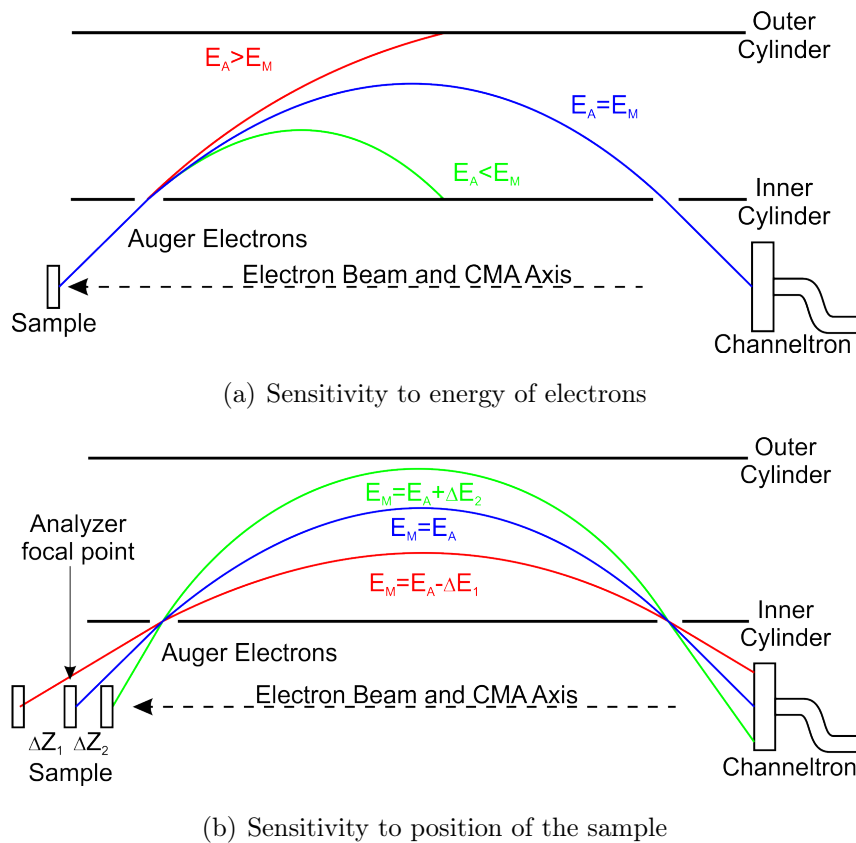g the sample surface with the analyzer focal point. E_A is the Auger electron energy and E_M the measured electron energy.[28]

12

AES can also be used to get a good approximation of the thickness of the deposited film. For this purpose a formula used in the Dissertation of D. Ullmann[29] for a MgO/Fe(001) system has been adjusted to account for the complex stoichiometry in BTO:

$$\frac{I_A}{I_B} = \frac{3}{5}\frac{S_A}{S_B}\left(\frac{1 - e^{-\frac{d}{\lambda_A \cos 42^\circ}}}{e^{-\frac{d}{\lambda_B \cos 42^\circ}}}\right) \tag{1.3}$$

with indices A and B for adsorbate and substrate, respectively. I is the measured Auger intensity, d the thickness of the adsorbate layer and λ the inelastic mean free path of electrons. S is the relative sensitivity of the Auger peak used for the calculation. The relative sensitivity is defined as the peak-to-peak amplitude of the element under investigation divided by the amplitude of a reference sample. The relative sensitivites used in this work have been taken from the *3rd. Edition* of the *Handbook of Auger Electron Spectroscopy*[28]. The reference peak is the Cu LMM transition ($922\,\text{eV}$) at $10\,\text{keV}$ primary beam energy.

1.3.2   Low Energy Electron Diffraction (LEED)

What Auger Electron Spectroscopy is for the composition of a surface Low Energy Electron Diffraction is for the structure: an easy and fast way to investigate. Another similarity with AES is the low penetration depth of only a few layers and thus a high surface sensitivity. A LEED image is the reciprocal image of the sample surface which contains information about the surface ordering over the coherence length of the electrons (typically $100\,\text{Å}$). In Figure 1.11(a) a well ordered unreconstructed surface of a clean Pd(001) crystal is shown, one can clearly see the sharp LEED spots where the Laue conditions are fulfilled. As comparison Figure 1.11(b) shows the clean surface of a Pt(001) crystal which is known to adopt this (5×20) reconstruction. Here a surface cell is much larger than the bulk unit cell covering 100 times the area (five times larger in a and 20 times larger in b direction).

The experimental setup to aquire these images consits of an electron gun for an electron beam with primary energies up to $500\,\text{eV}$ and a screen to display the Bragg diffraction spots. Such a system is schematically drawn in Figure 1.12. Electrons are emitted at the filament, collimated with the Wehnelt cylinder W

and accelerated with the potential difference between the cathode and A and D. B and C are used to focus the electron beam to improve the image quality. After diffraction occurs at the sample surface, the electrons are accelerated towards the fluorescent screen with a voltage of $5-7\,\text{kV}$ because only high-energy electrons can be made visible here. The suppressor voltage is applied to the middle grid in order to remove the inelastically scattered electrons which would otherwise produce a relatively homogeneous background illumination of the phosphor screen.
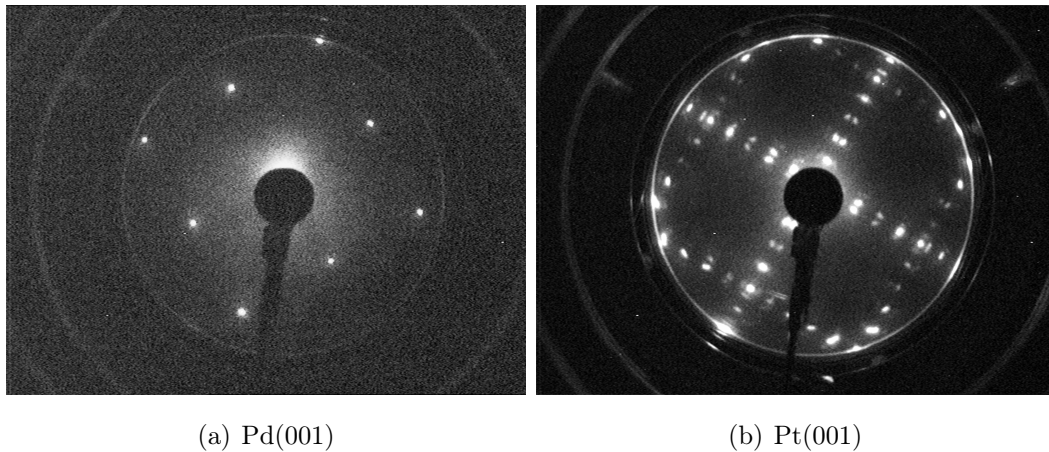

(a) Pd(001)   (b) Pt(001)

Figure 1.11: Comparison of the LEED images of clean crystal surfaces. a) shows an unreconstructed (1×1) surface of Pd(001) and b) the (5×20) reconstruction of clean Pt(001).
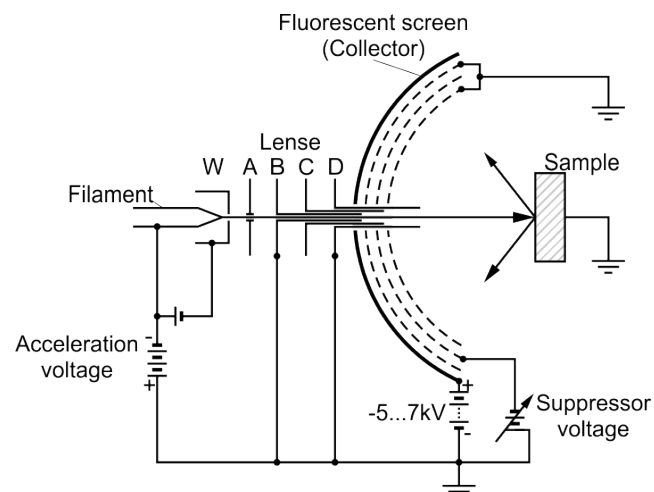
Figure 1.12: Schematic of three-grid LEED optics for electron diffraction experiments.[10]

1.3.3 Scanning Tunneling Microscopy (STM)

Scanning Tunneling Microscopy is a method for direct real space determination of the surface structure. Here a conducting tip is brought close to the sample surface and a bias voltage is applied (Figures 1.13 and 1.14). With the tip close enough to the surface, electrons will tunnel through the vacuum barrier and a current can be measured. A computer system stores voltage, current and tip position and scans the designated sample area by moving the tip along the surface either at a constant height or with a constant tunneling current. The former has the advantage of requiring less feedback interactions and being usually faster, but the latter is less likely to damage a surface with large height differences.

Computer: drives x,y scan; saves data; generates images.

Fine position & scanning are usually performed with one or more piezo-electric elements.

Coarse Approach

x,y

Feedback system: holds interaction between tip and surface constant.

Feedback Control

Fine Position

The coarse approach brings the tip and surface „close enough" for the fine mechanism to maintain a constant desired interaction.

Error Signal

Interaction Sensing

Tip

Tip-Surface Interaction

Surface

Figure 1.13: Schematic of a Scanning Probe Microscope. For STM the tip-surface interaction is the electron tunneling and the corresponding tunneling current is the signal for the feedback control.[30]

Tunneling is possible because the wave functions of the electrons in tip and sample extend into the vacuum and overlap at small tip-sample separation. In the tunneling barrier the tunneling probability decays exponentially and thus

the measured current also depends exponentially on the separation distance d:

$$I_T \sim \frac{U}{d} e^{-\kappa d \sqrt{\bar{\Phi}}}$$

(1.4)

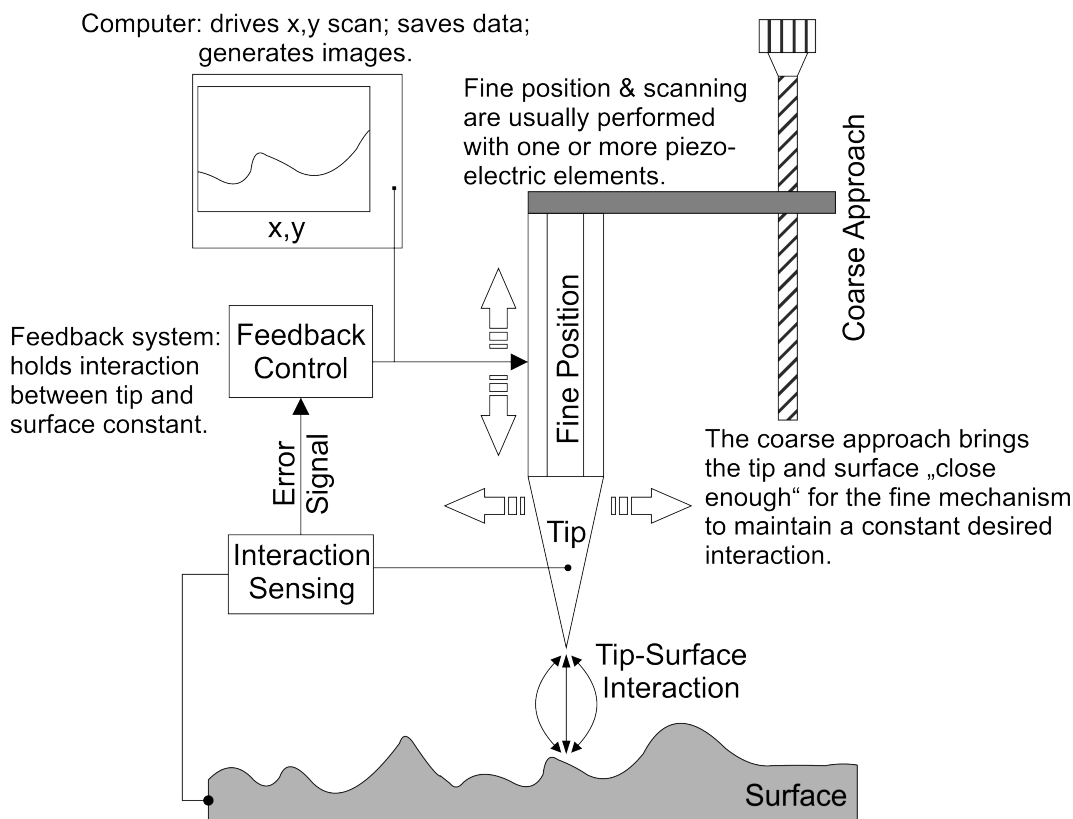where U is the applied voltage between tip and sample, $\bar{\Phi}$ their average work function ($\bar{\Phi} \gg eU$) and κ a constant with a value of about $1.025 \, \mathring{A}^{-1} \cdot (eV)^{-\frac{1}{2}}$ for a vacuum gap[10]. This exponential decay explains that only the outermost atoms of the tip take part in the tunneling and so a tip does not need to be perfectly sharp to achieve good resulution because there is usually only a single atom contributing to most of the measured current. On the other hand this dependence also explains the need for very clean measurement environments because the influence of unwanted adatoms propagating along the tip will disturb the measurement.
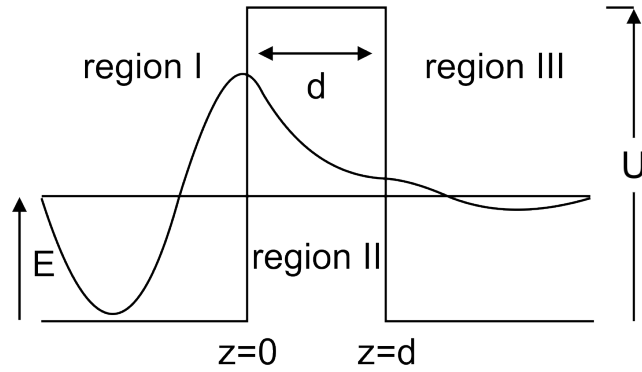
Figure 1.14: Electronic energy diagram for an STM showing the tunneling process. U is the height of the potential barrier, E is the energy of the incident electron, d is the thickness of the barrier.[30]

After the data has been collected the difficult task of analyzing has to be performed. The image presented by the computer system is not a topographical one, but a representation of the local density of states. For the case of a small bias voltage U an equation similar to Formula 1.4 is given by[31]

$$I \sim U \rho_s(0, E_f) e^{-\kappa d \sqrt{\bar{\Phi}}}$$

(1.5)

where ρ_s is the local density of states of the sample amd E_f the Fermi energy.

All these measurements and image interpretations have been performed on an Omicron LT STM using the native Omicron Control Software and the program WSxM.[32]

1.3.4 Surface X-Ray Diffraction (SXRD)

It is important to know the atomic structure if one wants to investigate the properties of a surface or interface. LEED is a good method to investigate the structure, but the strong interaction of electrons with the atoms composing the crystal structure leads to multiple scattering and this increases the difficulty of the investigation by a large amount. Analysis of the data is reduced to a complicated process of trial and error and large unit cells are almost impossible to model. X-Rays only weakly interact with matter and because of this the kinematic (single scattering) approach is sufficient for data analysis. Drawback of this weak interaction is the large penetration depth Λ_i leading to a large background signal due to thermal diffuse scattering from the bulk. This problem can be overcome by using Surface X-Ray Diffraction in the data acquisition. Here the penetration depth is limited by using a grazing incidence or exit geometry. It can be calculated by[13]:

$$\Lambda_i^{-1} = \sqrt{2} \frac{2\pi}{\lambda} \left(\sqrt{(\alpha_i^2 - \alpha_c^2)^2 + \left(\frac{\lambda\mu}{2\pi}\right)^2} + \alpha_c^2 - \alpha_i^2 \right)^{\frac{1}{2}} \tag{1.6}$$

where λ is the wavelength of the X-Rays, μ the linear absorption coefficient, α_i the incidence angle of the primary beam and α_c the critical angle for total external reflection. This function is shown in Figure 1.15 as a full line and the dashed line is $\frac{\sin\alpha_i}{\mu}$ as the penetration depth for large angles.

Another positive aspect is the fact that the refractive index for X-Rays of most materials is less than one and total external reflection at the surface is possible below a critical ange α_c[13]:

$$\cos\alpha_c = n = 1 - \frac{\lambda^2 e^2 F(0)}{2\pi m c^2 V} \tag{1.7}$$

where λ is the wavelength of the X-Rays, $F(0)$ the structure factor calculated at zero momentum transfer, c the speed of light, m and e the electronic mass and charge, respectively, and V the unit cell volume. For most materials the critical angle for X-Ray wavelengths is in the range of $0.1° < \alpha_c < 0.9°$. Measuring at this angle enhances the surface signal by a factor of 4 according to the formula for the transmission coefficient $|T_i|^2$ combined with the previous equation 1.7 [13, 33]:

$$|T_i|^2 = \left| \frac{2\sin\alpha}{\sin\alpha + \sqrt{n^2 - \cos^2\alpha}} \right|^2 \tag{1.8}$$
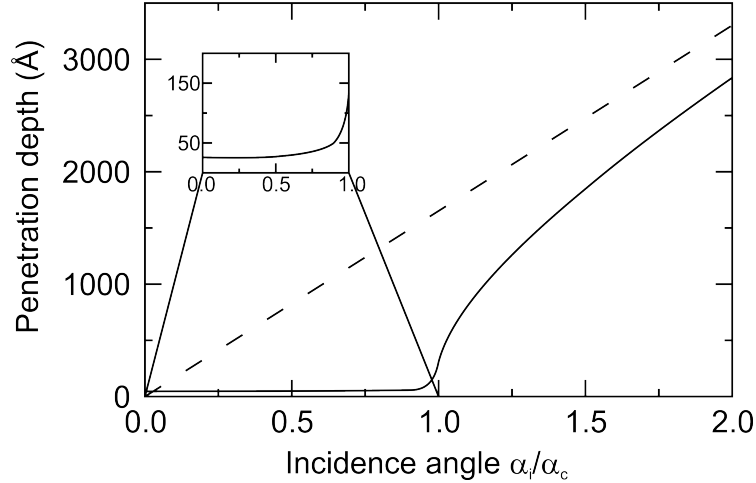
Figure 1.15: $\frac{1}{e}$ depth of penetration normal to the surface of an incoming beam with wavelength $\lambda = 1.38\,\text{Å}$ upon a Ge surface as a function of angle of incidence. The full line is given by equation 1.6, the broken line is $\Lambda_i = \frac{\sin \alpha_i}{\mu}$. The critical angle is $\alpha_c = 0.284°$.[13]

In Figure 1.16 this is shown for the example of a clean InSb($\bar{1}\bar{1}\bar{1}$)-(3x3) surface. Theoretically one could achieve the same signal enhancement by also measuring with grazing exit angle, but to measure all the necessary data one of the two has to be varied.

The measured intensity is proportional to the square of the absolute amplitude of the structure factor of the sample. This structure factor contains all the information about the atomic geometry inside the unit cell and can be derived by starting with the Thomson formula explaining the scattering by an electron at position $\vec{r}$ measured at a distance R [15]:

$$A_e e^{-i\vec{k}_1 \cdot \vec{r}} = A_0 e^{i\vec{k} \cdot \vec{r}} \frac{e^2}{mc^2 R} \tag{1.9}$$

with $A_0 e^{i\vec{k} \cdot \vec{r}}$ the incident plane-wave amplitude and A_0^2 the incident intensity in $\frac{\text{photons}}{\text{unit area} \cdot s}$. Expanding this formula to an atom by integrating over its electron density leads to the following expression:

$$A_a = A_0 \frac{e^2}{mc^2 R} \int e^{i\vec{q} \cdot (\vec{r} + \vec{r}')} \varrho(\vec{r}') \mathrm{d}^3 \vec{r}' = A_0 \frac{e^2}{mc^2 R} f(\vec{q}) e^{i\vec{q} \cdot \vec{r}} \tag{1.10}$$

with the atomic form factor $f(\vec{q})$ as the Fourier transform of the electronic distribution function $\varrho(\vec{r}')$ and $\vec{q} = \vec{k}_f - \vec{k}_i$ the momentum transfer between incident and exit wave vectors ($\vec{k}_i$ and $\vec{k}_f$). The form factor describes the scattering of a single atom and one has to calculate the sum of all the individual
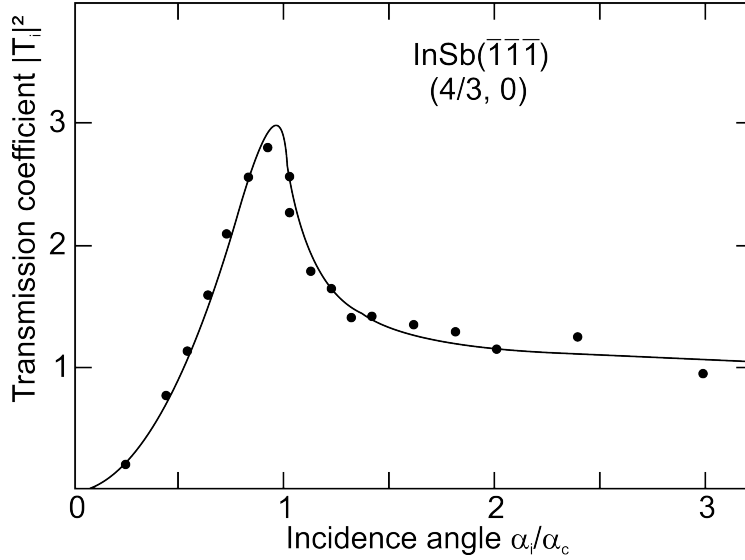
Figure 1.16: Transmission coefficient $|T_1|^2$ as a function of incidence angle α_i. The curve is shown for an InSb($\bar{1}\bar{1}\bar{1}$) surface and a wavelength $\lambda = 1.2\,\text{Å}$, the critical angle is $\alpha_c = 0.25°$. The experimental points are from the (4/3,0) reflection of the InSb($\bar{1}\bar{1}\bar{1}$)-(3x3) surface normalized to the correct scale. The intensity of a superlattice reflection is a measure of the intensity of the evanescent wave and hence of the transmission coefficient.[13]

atoms to get the diffracted amplitude of the unit cell which is described by the structure factor $F(\vec{q})$:

$$A_c = A_0 \frac{e^2}{mc^2 R} \sum_{j=1}^{N_c} f_j(\vec{q}) e^{i\vec{q}\cdot\vec{r}_j} = A_0 \frac{e^2}{mc^2 R} F(\vec{q}) \qquad (1.11)$$

The sum can be expanded to account for thermal vibrations of the atoms by including the Debye-Waller factor $e^{-B_j(q/(4\pi))^2}$.

The intensity of a wave diffracted by multiple unit cells is strongly peaked when the Laue conditions are fulfilled just like it is in an infinite three-dimensional crystal with the exception, that the diffraction intensity between the Bragg points in the direction along the surface normal is not vanishing. This non-vanishing intensity leads to Crystal Truncation Rods (CTRs), two-dimensional diffraction features that arise from bulk crystals terminated by a sharp boundary (Figure 1.17(a) shows this for a primitive cubic crystal lattice where the Laue conditions are fulfilled for $h, k, l \in \mathbb{Z}$). A CTR with only bulk contributions has a characteristic $\sin^{-2}(\frac{1}{2}q_3 a_3)$ shape and its intensity is given by:

$$I_b \left(\frac{2\pi h}{a_1}, \frac{2\pi k}{a_2}, q_3 \right) = A_0^2 \frac{e^4}{m^2 c^4 R^2} |F|^2 N_1^2 N_2^2 \frac{1}{4 \sin^2(\frac{1}{2}q_3 a_3)} \qquad (1.12)$$

where the last part comes from the summation over all unit cells of the crystal. The CTRs contain information about the roughness of the surface and the structure of the investigated interface. Roughness of a surface decreases the intensity between the Bragg peaks whereas the interface can be calculated from the overlay of bulk and surface signal.

If an $(n \times m)$ reconstructed surface is present additional Superlattice Rods (SLRs) at positions with $(\frac{i}{n}, \frac{i}{m})$ with $i \in \mathbb{Z}$ appear (Figure 1.17(c)). These contain only information about the reconstructed part of the surface without bulk contribution except for the integer rods where SLR and CTR overlap. This can be used to investigate the surface independent of the interface to the bulk crystal decreasing the amount of atoms in the structure model. Furthermore this is the reason for the high surface sensitiviy despite the deep penetration depth of the X-rays. One selects areas in the reciprocal space for analysis which contain the necessary information (called Fourier Filtering) and discards the Bragg peaks themselves, since all the surface information is hidden due to the high bulk contribution. After the model has been thoroughly fitted the inclusion of integer order rods adds information about the registry between surface and bulk. An example of the SLR/CTR overlap can be seen in Figure 1.18 with the Crystal Truncation Rod of a covered Palladium crystal. Here additional peaks are present between the Bragg peaks at (110) and (112) by the $BaTiO_3$.

Measuring intensities only leads to the amplitude of the structure factor, the phase information is lost. Reconstructing this phase information is the task of data analysis.
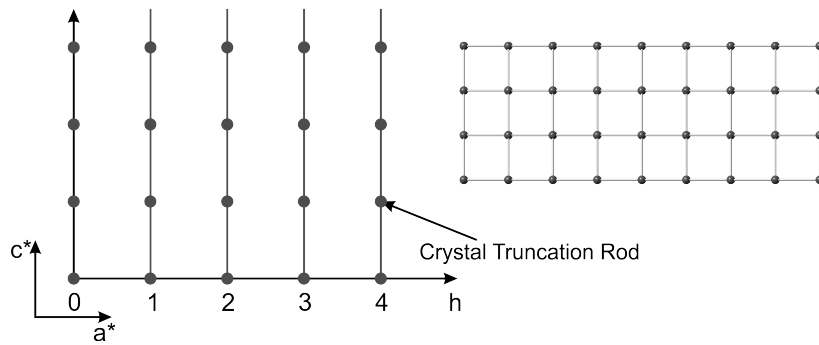
(a) Clean, flat surface
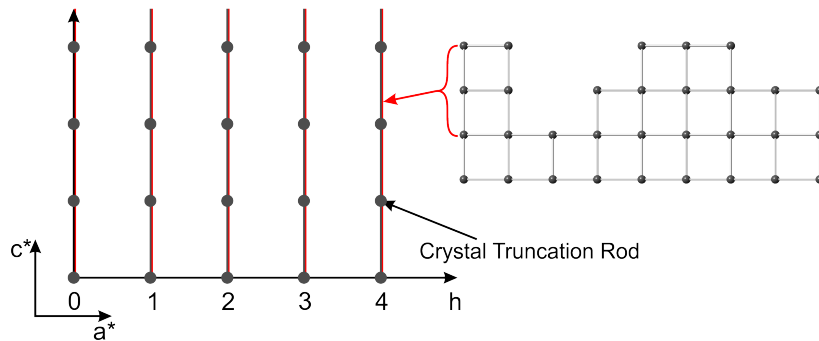
(b) Disordered or rough surface
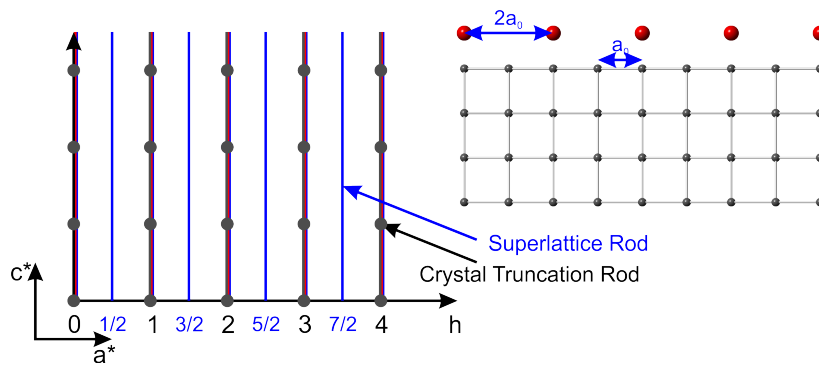
(c) Reconstructed surface

Figure 1.17: Schematic showing CTRs and SLRs for a simple cubic crystal surface. a) A clean, flat surface gives rise to CTRs at positions with $h, k \in \mathbb{Z}$ and peaks where the Laue conditions are fulfilled. b) Rough surface's rods are changed by decreased intensity between the Bragg peaks. c) $(n \times m)$ reconstructed surfaces gain SLRs at $(\frac{i}{n}, \frac{i}{m})$ with $i \in \mathbb{Z}$. These rods contain information about the reconstructed part of the surface and in the case of rational periodicity they overlap with the integer order CTRs and modulate their intensity.
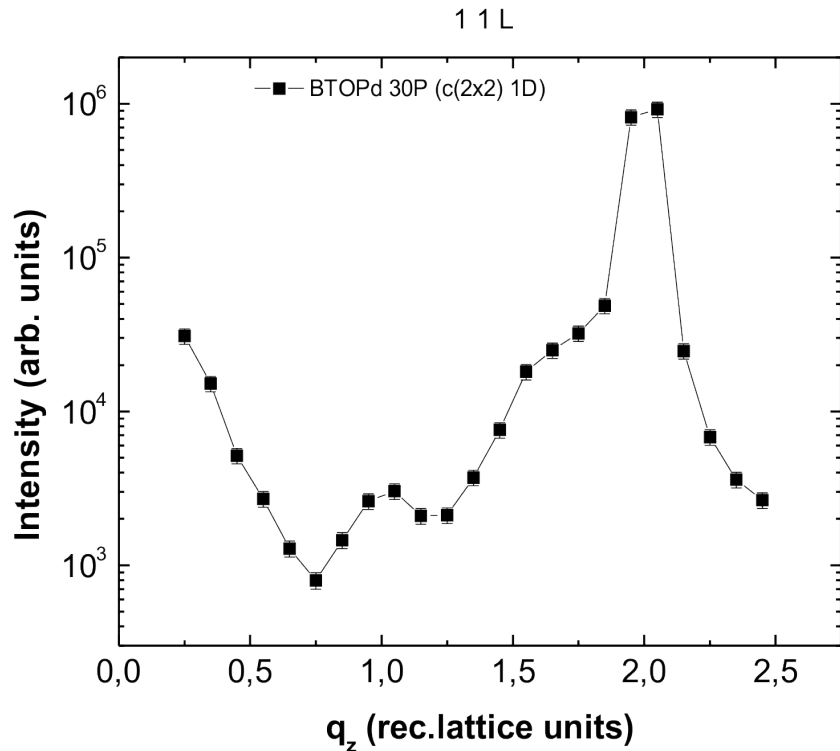
Figure 1.18: Example of a $(11L)$ Crystal Truncation Rod from a Barium Titanate covered Palladium sample with Bragg peaks at $L = 0$ and $L = 2$. Additional peaks arise from additional layers taking part in the surface reconstruction.

1.3.4.1 Acquisition of SXRD-Data

To acquire the datapoints necessary for analysis one needs a suitable diffractometer similar to the schematic in Figure 1.19. It has to be set up in such a way, that the incidence angle can be kept constant by precise alignment of the sample surface. This requires adjusting θ while rotating around the sample normal ϕ because the sample surface is usually not perfectly parallel to the mounting stage due to miscut. The angles α_f and ϕ_D describing the detector position require a movement range as large as possible thus increasing the accessible area in the reciprocal space. These angles are not only restricted by the diffractometer but also by the exit window of the vacuum chamber, creating the necessity for this window to be as large as possible, with a hemisphere of a Beryllium being one of the best, structurally possible solutions. All the rotation stages need high precision to increase the quality of the measurements

by minimizing misalignment.
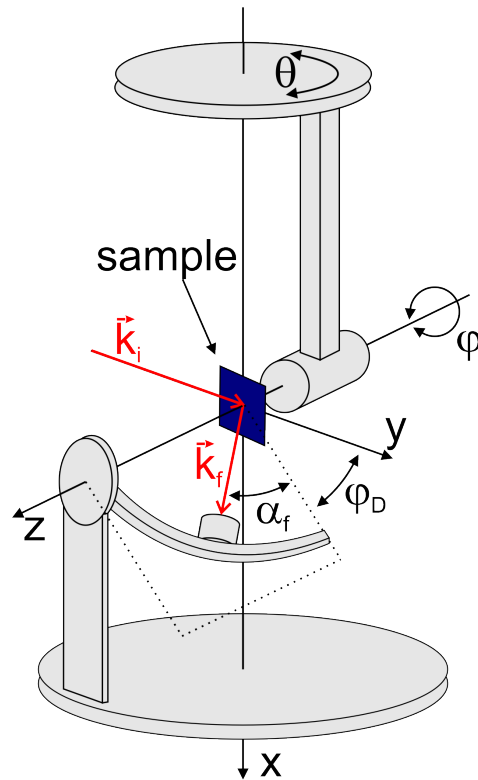
Figure 1.19: Diffractometer for Surface X-Ray Diffraction with all the relevant angles marked in the schematic.

The next important part for data aquisition is the detector which traditionally is a point detector since it is lightweight and easy to operate. Measuring the intensity with a point detector is usually performed with a scan starting away from the Bragg peak at background level and moving through the peak by rotating the sample around its normal direction. When the measured intensity is again at background level the peak is integrated and background subtracted using the following formula, where S_i and B_i are data points with a peak signal and background, respectively, N_S and N_B are the number of corresponding data points[15]:

$$I = \sum_i S_i - \frac{N_S}{N_B} \sum_i B_i \qquad (1.13)$$
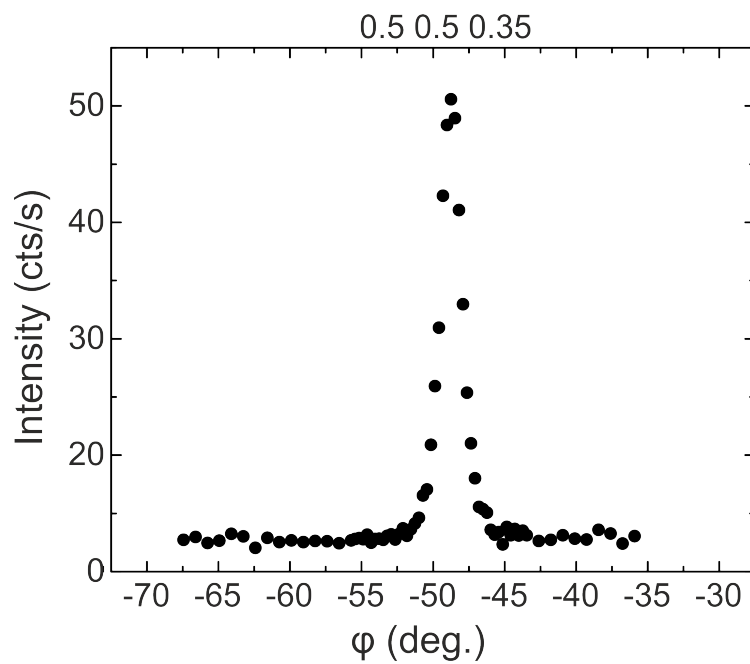
(a) Rocking scan
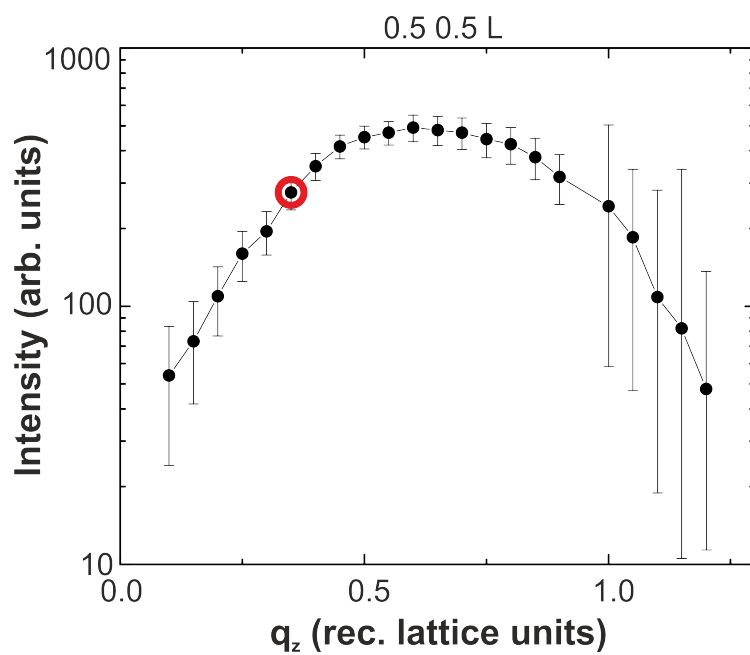
(b) Superlattice Rod

Figure 1.20: Measurement of a 1uc thick layer of $BaTiO_3$ on a clean Fe(001) single crystal. a) A rocking scan around the surface normal φ is necessary to measure a slice of the whole rod. b) Integrating the peak from the rocking scan leads to the data point marked with a red circle.

Figure 1.20 shows the result of such a measurement. The upper image shows the rocking scan performed by rotating the sample around its surface normal φ with the strong peak at 47° and the low background. Integrating this scan and removing the background leads to the data point inside the red circle in the second image. The data was taken on a $BaTiO_3$/Fe(001) interface with a thickness of one unit cell (uc) $BaTiO_3$. Since it is an SLR of such a thin film the measurement in these cases can take up to a few hours for the whole rod.

This process can be sped up by using an area detector like the one shown in Figure 1.21. Here the rocking scan is averted by measuring the whole rod profile in one image and the integration is done with the whole profile and not only a slice, thus increasing the data quality at the same time as the measurement speed. Figure 1.22 shows such a two dimensional image.
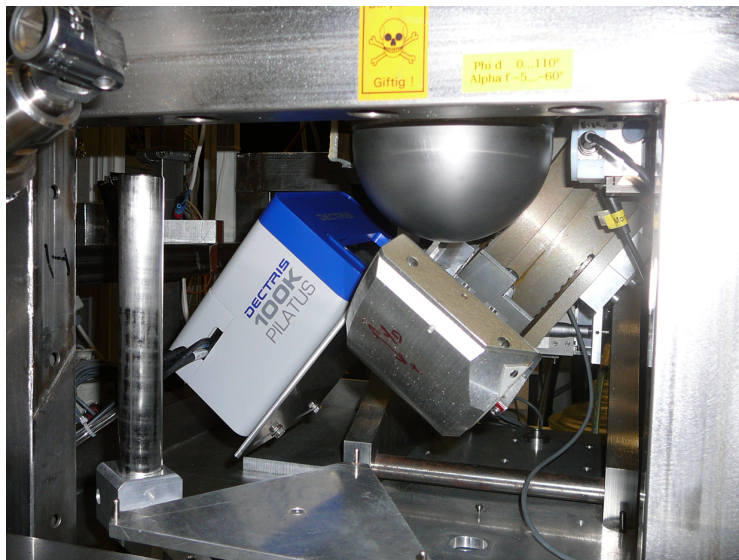
Figure 1.21: Image of the Pilatus II 100k pixel detector[34–36], showing the Beryllium hemisphere for in situ X-Ray measurements.

The more complicated integration of the area detector data is performed by a MATLAB® [37] routine written by C. Schlepütz [38] specifically for the Pilatus.

A possible way to increase the quality of the measured data is by measuring symmetry equivalent datapoints. Since the disagreement between these points is a measure of systematic errors, typically less than 10%, one can use the disparity to check the alignment and quality of the crystal. Furthermore averaging these datapoints can identify unwanted spikes created by stray radiation
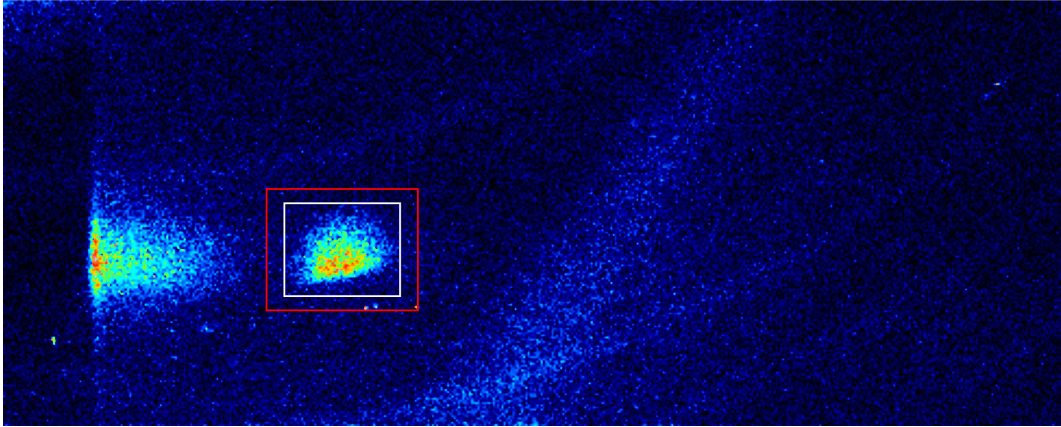
Figure 1.22: Visual representation of an image taken with an area detector. The count rate is stored in a 32bit color coded image which can be analysed with corresponding software. Displayed is the measurement of a $(10l)$ rod of $4\,\mathrm{uc}$ of $BaTiO_3/Fe(001)$ at a position of $l = 0.4\,\mathrm{r.l.u.}$ (reciprocal lattice units). The white and red rectangles correspond to the area of integration for the peak and background, respectively. The additional peak to the left is the total reflected beam. Additional blue and purple streaks are unwanted signals from the system and they cannot be reduced further, but by carefully positioning the signal and background boxes these will be removed through background subtraction.

and aid in the elimination of errors these produce.

The final step before analysis of the data is the application of geometrical correction factors to the measured intensities. The first is the Lorentz factor correction which for the open slit geometry of the area detector amounts to $L = \frac{1}{\sin(\alpha_f)}$ and for the point detector it requires a more complicated calculation following the work of Schamper *et al.*[39] Further correction factors have to account for the polarization of the X-ray light used and the illuminated sample area. The value of the polarization factor P is dependent upon the diffractometer geometry and the polarization of the X-ray source (high polarization for a beamline and unpolarized for a rotating anode). The area factor A depends on the slit geometry and the beam footprint on the sample. Combining all the correction factors leads to the following expression for the experimentally observed square of the structure factor amplitudes used for the analysis:

$$|F_{obs}|^2 \sim \frac{I}{P \cdot A \cdot L} \tag{1.14}$$

1.3.4.2 Analysis of measured Data

Analysis of the data is based on the comparison of calculated structure factor amplitudes based on the structure model with the measured structure factor amplitudes using computer assisted refinement of the model to achieve sufficient agreement. The refinement is performed by the program system PROMETHEUS[40] using the least-squares method. The quality of the fit is quantified by the goodness of fit (square root of the reduced χ^2 shown in Equation 1.15) and the unweighted residuum (Equation 1.16). For both cases a smaller number indicates a better fit with the former being in the vicinity of 1 indicating that the model is within the experimental data's error. For the unweighted residuum values between 10% and 15% already show a reasonable fit and only rare cases have values smaller than these.

$$GoF = \sqrt{\chi^2} = \sqrt{\frac{1}{N-p} \sum \frac{(|F_{obs}| - |F_{calc}|)^2}{\sigma^2}} \qquad (1.15)$$

$$R_u = \frac{\sum ||F_{calc}| - |F_{obs}||}{\sum |F_{obs}|} \qquad (1.16)$$

In both equations $|F_{calc}|$ and $|F_{obs}|$ are the structure factor amplitudess for the calculated model and the experimentally measured data, respectively. N is the number of measured structure factors, p the number of free parameters used in the model and σ describes the uncertainties in the measured structure factors.[13, 41]

A method to create a starting model for structure analysis is using the z-projected two-dimensional Patterson function[15, 42]:

$$P(x, y) = \sum_{hk} |F_{hk}|^2 \cos \left[2\pi(hx + ky) \right] \qquad (1.17a)$$

$$\sim \int_0^{a_1} \int_0^{a_2} \rho_0(r_1, r_2) \rho_0(r_1 + a_1 x, r_2 + a_2 y) \mathrm{d}r_1 \mathrm{d}r_2 \qquad (1.17b)$$

This function in combination with the in-plane structure factors can be represented as a contour map with the symmetry of the surface reconstruction. In this contour map the peaks correspond to the interatomic vectors in the unit cell, not to the atomic positions themselves. Thus there is always a

dominant peak at the (0,0) position accounting for the vector pointing from an atom to itself. Figure 1.23 is a contour map calculated using the Patterson function and the in-plane structure factors from the (2×1) reconstruction of an annealed $BaTiO_3$ single crystal. One can see positive (solid lines) and negative maxima (dashed lines) corresponding to vectors pointing to atoms and vacancies, respectively. This happens because only fractional order rods have been used in the calculation and this leads to the map showing the interatomic vectors of the (2×1) cell relative to the (1×1) structure. With this information one can try to deduce a model in which the vectors related to the negative peaks correspond to an atom/vacancy correlation.
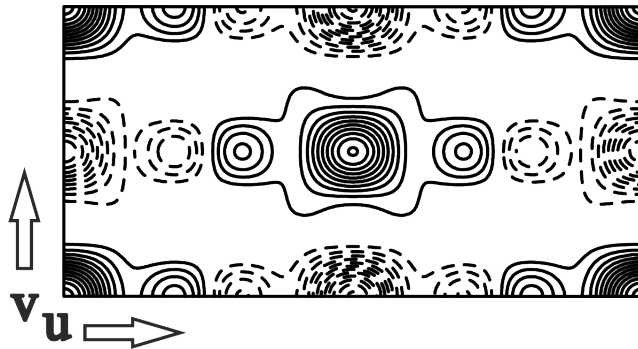
Figure 1.23: Contour map calculated using the Patterson function. Solid and dashed lines depict positive and negative maxima, respectively, which define vectors pointing from one atom to either another atom or a vacancy.[43]

Creating this model is a process of continuously adjusting the starting values of the in-plane values for the structure suggested by the Patterson map and using the computer software to compare this to the measured in-plane structure factor amplitudes and further refine the data. After repeating this process enough times a model for the starting point should have been found. This model has good values for the in-plane interatomic distances but no information about the distances perpendicular to the surface. Gathering this information is done in the analysis including the higher l-values of the Superlattice Rods. After thorough analysis of the reconstruction one needs to include the Crystal Truncation Rods in further calculations in order to correctly place the reconstructed layers atop the bulk crystal.

If enough information about the investigated surface is already present, one can skip the preliminary refinement steps and start with the full dataset. This

leads to a complex refinement with five degrees of freedom per unit cell atom (atom position in three directions, site occupancy and thermal motion), an even larger number of degrees of freedom has to be considered if the Debye-Waller-factor for thermal motion is not isotropic. Investigating such a structure requires intelligent placement of restraints in order to decrease the number of free parameters. These restraints, like the in-plane positions can come from preliminary investigations if performed or from prior knowledge of the registry. Further possibilities are collective change of atom parameters by linking their position or thermal movement and if possible, the simplest way to decrease the free parameters is usage of plane group symmetry[44] to decrease the number of independent atoms in the unit cell.

The final result of this analysis should be a physically reasonable structure with an R-value as small as possible, ideally less than 10%, and a GoF close to 1. If this is achieved one has a very good starting point for the comparison with theory and other experiments in order to prove the results.

Chapter 2

Experiment

The experimental investigations of ultrathin Barium Titanate films have been performed on single crystals of Fe(001), Pd(001) and Pt(001) shown in sections 2.1.1, 2.1.2 and 2.1.3, respectively. In addition to measurements of $BaTiO_3$ on a metal surface, a metal (in this case Fe) has been deposited and studied on a film and on a single crystal of $BaTiO_3$ in section 2.2. Furthermore, SXRD measurements on the clean surface of a (2x1) reconstructed $BaTiO_3(001)$ crystal have been performed and are shown in section 2.3.

All samples have been cleaned before deposition, with the Fe(001) preparation following the method explained by Kirschner[45] in all chambers used for the measurements. Failing to provide the flash capabilities necessary for the preparation of $BaTiO_3(001)$-(2x1) and Pt(001)-(5x20) in the in-house SXRD chamber (Figure 2.1), those samples have only been investigated by STM locally and the SXRD measurements have been performed at the European Synchrotron Radiation Facility (ESRF), Grenoble, France using beamlines ID03 and ID32 respectively. Fe(001) and Pd(001) have been investigated locally and at ID32 at ESRF.

After sputter cleaning and annealing the samples, the structure composition and quality have been checked using AES and LEED. Deposition of $BaTiO_3$ on a surface with good enough quality was performed by using PLD or thermal evaporation. Equation 1.3 was used to estimate the layer thickness with AES and annealing was performed with concurrent LEED investigations until a good c(2x2) reconstruction of the $BaTiO_3$/metal system was found. When the preparation efforts resulted in a well ordered $BaTiO_3$ film it was measured by
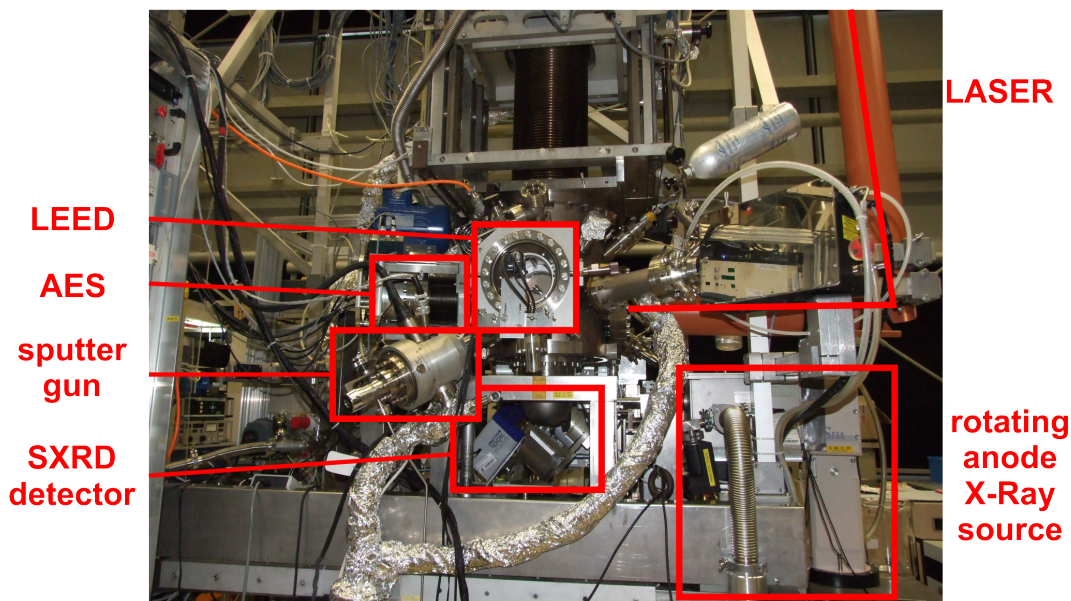
Figure 2.1: Picture of the in-house in-situ SXRD chamber at the Max-Planck-Institute of Microstructure Physics in Halle, Germany. Important features of the system are shown in red borders.

using either the in-house rotating anode or the beamlines at the ESRF.

This chapter features a large amount of structure models and in order to distinguish the different atoms and compare different structure models visually a convention has been utilized. This convention uses the ionic radii of the elements to separate them by size and the following color scheme to enhance this separation. The metal atoms of the underlying crystals all use slightly different shades of gray.
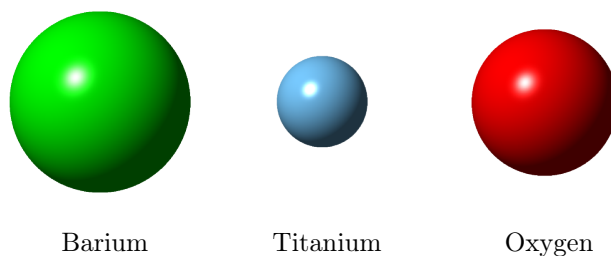
Figure 2.2: Coloring scheme and comparison of relative sizes for the elements used in the structure models.

Additionally included is a collection of models showing the coverage per-

centage of the separate BaTiO$_3$ unit cell layers. Coverage percentages are rounded to multiples of 10% (experimental accuracy) and displayed graphically by defining 10% of coverage as one block of BaO or TiO$_2$. These models are supposed to be a simple visible representation and no information about island sizes is included.

2.1 BaTiO$_3$(001) on the (001) surface of different metals

The first part of the experimental work was performed on the BaTiO$_3$/metal interface. The metal crystals in this work are Fe(001), Pd(001) and Pt(001) and they were chosen because of their small difference in lattice misfit m with tetragonal bulk BaTiO$_3$ of -1.5%, 2.6% and 1.7%, respectively.

$$m = \frac{a_{\mathrm{BTO}} - a_{\mathrm{metal}}}{a_{\mathrm{metal}}} \qquad (2.1)$$

2.1.1 BaTiO$_3$(001)-c(2×2)/Fe(001)

On the Fe(001) crystal films with average thicknesses between 0.5 uc (unit cells) and 4 uc have been deposited, both in an oxygen atmosphere and without additional oxygen. Since deposition in oxygen did not lead to a well ordered structure after annealing (Figure 2.3) further depositions with PLD were performed without additional oxygen. All depositions were done with the sample at room temperature and after annealing the films usually showed a c(2×2) reconstruction with thicker films requiring higher annealing temperatures or multiple cycles of depositing a small amount and annealing the sample. The LEED image of such a sample is shown in Figure 2.4 in comparison to the clean Fe crystal.

Figure 2.5 shows an example of the BaTiO$_3$ structure on a Fe(001) crystal. In this view along the [00$\bar{1}$] direction the squares represent the surface unit cell of bcc Fe(001) (black) and the unit cell of BaTiO$_3$ leading to the c(2×2) reconstruction. The darker and lighter grey spheres belong to the surface and first sub-surface layer of the Iron crystal, respectively. As mentioned in the previous chapter, a superlattice on the surface with a larger periodicity leads to shorter reciprocal distances, visible in the LEED. The surface unit cell of
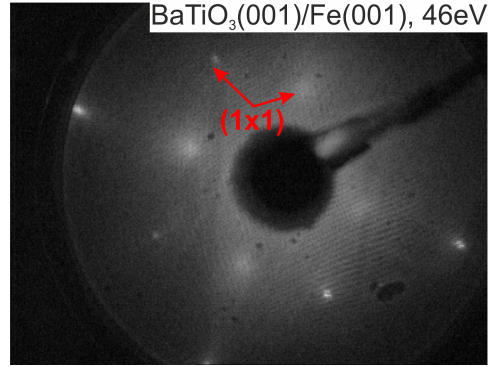
Figure 2.3: LEED image of a $BaTiO_3$/Fe system deposited with PLD in an oxygen atmosphere of $5 \cdot 10^{-7}$ mbar.
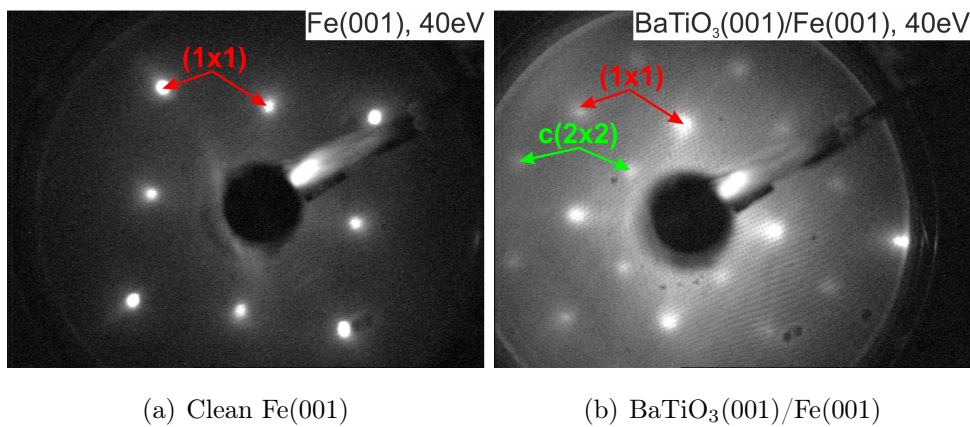
(a) Clean Fe(001)   (b) $BaTiO_3(001)$/Fe(001)

Figure 2.4: LEED comparison of the clean and film covered surface of Fe(001). The covered surface shows additional spots corresponding to a $c(2 \times 2)$ reconstruction.

$BaTiO_3(001)$-$c(2 \times 2)$ is shown with the red square occupying four times the area of the bcc Fe(001) cell. Shown in blue is the $(\sqrt{2} \times \sqrt{2})R45°$ surface unit cell of $BaTiO_3$ which can be used equivalently to $c(2 \times 2)$ in order to describe the $BaTiO_3$/Fe(001) system. Using this second surface cell for the analysis has the advantage of decreasing the amount of atoms to be considered in the calculations due to its smaller size.

For further investigation three samples were chosen with coverages of 0.8 uc, 1.6 uc and 2.7 uc which for simplicity's sake will be labeled as 1Fe, 2Fe and 3Fe for samples with 1, 2 and 3 unit cells, respectively. Figure 2.6 shows a compilation of the experimental (symbols) and calculated (lines) structure factor amplitudes for these three samples. The magnitude of the error bars arises from the reproducibility of symmetry equivalent reflections (for example
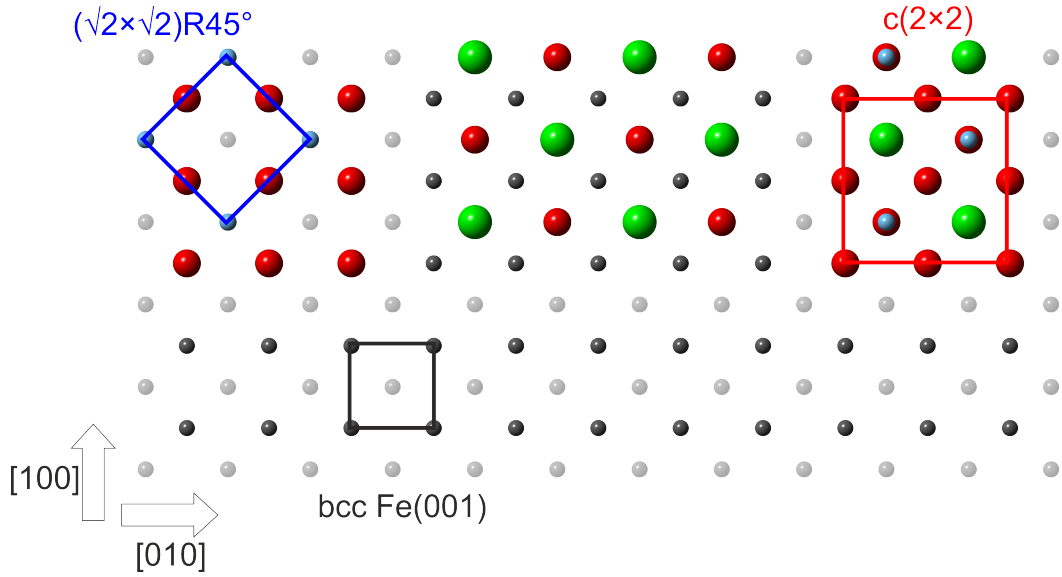
Figure 2.5: Top view schematic of $BaTiO_3$ on an Fe(001) crystal. The structures shown are (from left to right): TiO_2 layer (blue/red), BaO layer (green/red) and TiO_2/BaO stack. The square boxes represent the different surface unit cells: black shows the bcc Fe(001) unit cell and red is the c(2 × 2) unit cell of $BaTiO_3$/Fe(001). For the calculations the smaller $(\sqrt{2} \times \sqrt{2})$R45° unit cell was used which is indicated by the blue box.

(1 0 L), (0 1 L), (0 $\bar{1}$ L) and ($\bar{1}$ 0 L); in all cases about $10 - 15\%$) and the 1σ standard derivation from the counting statistics.

Clearly visible in the diagrams is a sharpening of the fractional order rods' peaks (left) with increasing thickness of the film, which is described by the Scherrer Equation[46]. Furthermore, the amount of peaks in the reciprocal space increases with the number of scattering layers which is best visible for integer order rods but also occurs for the fractional order rods. The quality of the fits were good, indicated by $R_u = 0.10 - 0.13$ for all three samples. The uncertainty of the atomic positions for samples 1Fe and 2Fe is approximately 0.10 Å and for sample 3Fe it is in the range of $0.15 - 0.20$ Å. This uncertainty is influenced by the element and the occupancy of the scattering atoms in such a way, that the heavier Barium or a higher occupancy has a stronger impact on the accuracy than the lighter Oxygen or a less filled layer. Thus the low occupancy of the individual layers in the 3Fe sample leads to the large uncertainty and the accuracy of the Oxygen positions is always worse than that of the metal atoms.
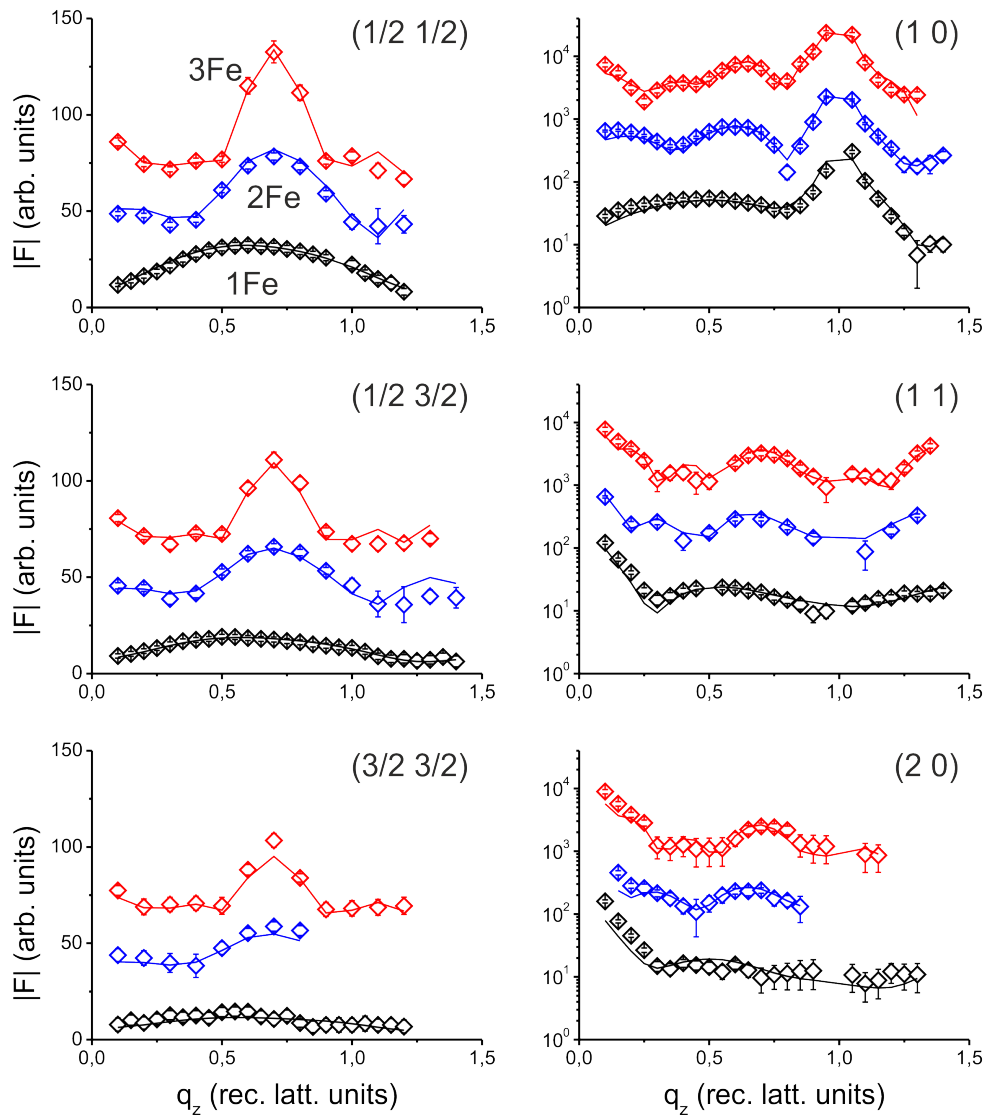
Figure 2.6: Fractional (left, linear scale) and integer order (right, logarithmic scale) rods of the three investigated Fe(001) samples (1Fe, 2Fe and 3Fe with black, blue and red diamonds, respectively). Shown are the measured data points as symbols and the calculated structure factor amplitudes as lines. The curves have been shifted to clearly separate them.[47]

Sample 1Fe

Starting with sample 1Fe (the thinnest layer) a structure model has been developed which is shown in Figure 2.7. The first important feature to note is that the $BaTiO_3$ forms a bilayer of TiO_2-BaO without breaking up into separate layers and that there is no indication of three dimensional island growth present.

(a) model

(b) coverage

Figure 2.7: Structure model for the $BaTiO_3(001)$-$c(2\times2)$/Fe(001) sample with a thickness of $0.8\,uc$. All values in Ångström, $\Delta\delta = 0.10\,\text{Å}$.

The next feature is that the TiO_2 layer forms the interfacial layer between $BaTiO_3$ and Fe with the oxygen atoms placed directly above the Fe atoms as predicted by theory.[5, 48] Although Fechner *et al.* calculated the case of a thin Fe layer atop a TiO_2-terminated $BaTiO_3$ crystal[48] their Fe-O bond distance is just as small as the one in the presented model with $1.78\,\text{Å}$ which is relatively short. The Ba-O bond distances inside the BaO layer are fairly close to the bulk values of tetragonal $BaTiO_3$ with $2.87\,\text{Å}$ compared to $2.824\,\text{Å}$ for the bulk value[16] and the Ba-O bonds between the planes are enlarged by about 6% from $2.796\,\text{Å}$ in the bulk to $2.96\,\text{Å}$.

The Ti-O bond lengths show the same behavior as the in-plane distances

being fairly close to the bulk value differing only because of the -1.5% lattice misfit between $BaTiO_3$ and Fe. The out-of-plane distances are elongated by an even larger amount than the Ba-O distances. The change is about 10% compared to the longer Ti-O out-of-plane distance in the tetragonal bulk crystal (model: $2.39\,\text{Å}$, bulk: $2.169\,\text{Å}$ and $1.867\,\text{Å}$), but this is harder to compare, since the bulk Ti atom is shifted out of the TiO plane by $0.115\,\text{Å}$[16] which is not present in the 1Fe sample ($\delta = 0.00 \pm 0.10\,\text{Å}$). The vertical shift δ in this work is defined as the vertical distance between the oxygen plane and the metal atoms of the same layer with δ being negative when the metal is below the oxygen plane. Opposed to this vanishing shift the BaO layer shows a very large δ of $-0.23 \pm 0.10\,\text{Å}$. The reason for this large negative value in the top interface layer will be shown in the discussion at the end of the section.

Sample 2Fe

The next sample, 2Fe, has a closed unit cell layer at the interface and a partially filled unit cell layer on top (Figure 2.8). This implies that the structure grows according to either Frank-van der Merwe or Stranski-Krastanov growth.

This model is in many ways similar to the thinner film. A TiO_2 layer is at the interface to Fe and BaO at the film surface, the Fe-O bond length is comparably short and the δ at the film surface is still negative, albeit smaller with $-0.16 \pm 0.10\,\text{Å}$. Furthermore, the distance between the interfacial TiO_2 layer and the adjacent BaO is similar to the previous sample. Differences arise from the fact, that the TiO_2 layers in this film show a very large vertical shift with $\delta = 0.46 \pm 0.10\,\text{Å}$ leading to an alternating direction of δ in adjacent layers. Additionally its value is not only alternating in direction, but also in magnitude (large positive δ for TiO_2 and smaller negative δ for BaO). Because of this the Ti-O bond length between the layers is alternating between $1.74\,\text{Å}$ for layers #1-#2 and #3-#4 and $2.49\,\text{Å}$ for layers #2-#3, although the vertical O-O distances stay relatively constant ($2.20\,\text{Å}$, $2.03\,\text{Å}$ and $2.20\,\text{Å}$ from bottom to top). The latter is the same for the vertical Ba-O distances ($2.87\,\text{Å}$, $2.99\,\text{Å}$ and $2.87\,\text{Å}$). Figure 1.2(b) in chapter 1.1 shows the δ of all layers with the same sign which is contrary to these results but not surprising since the properties of thin films often differ from the bulk state.

(a) model

(b) coverage

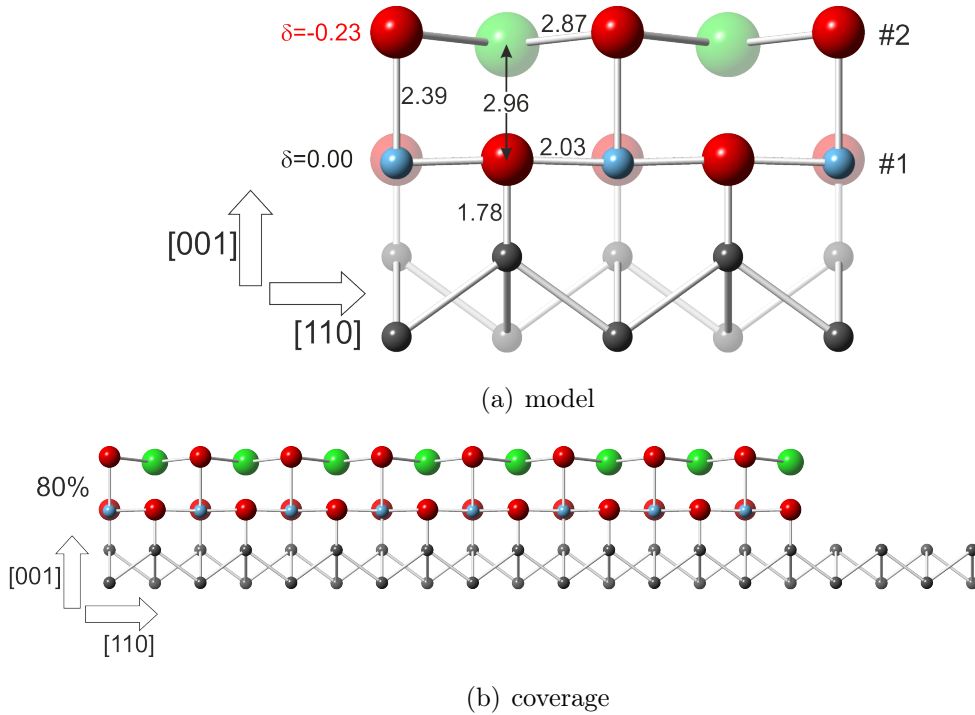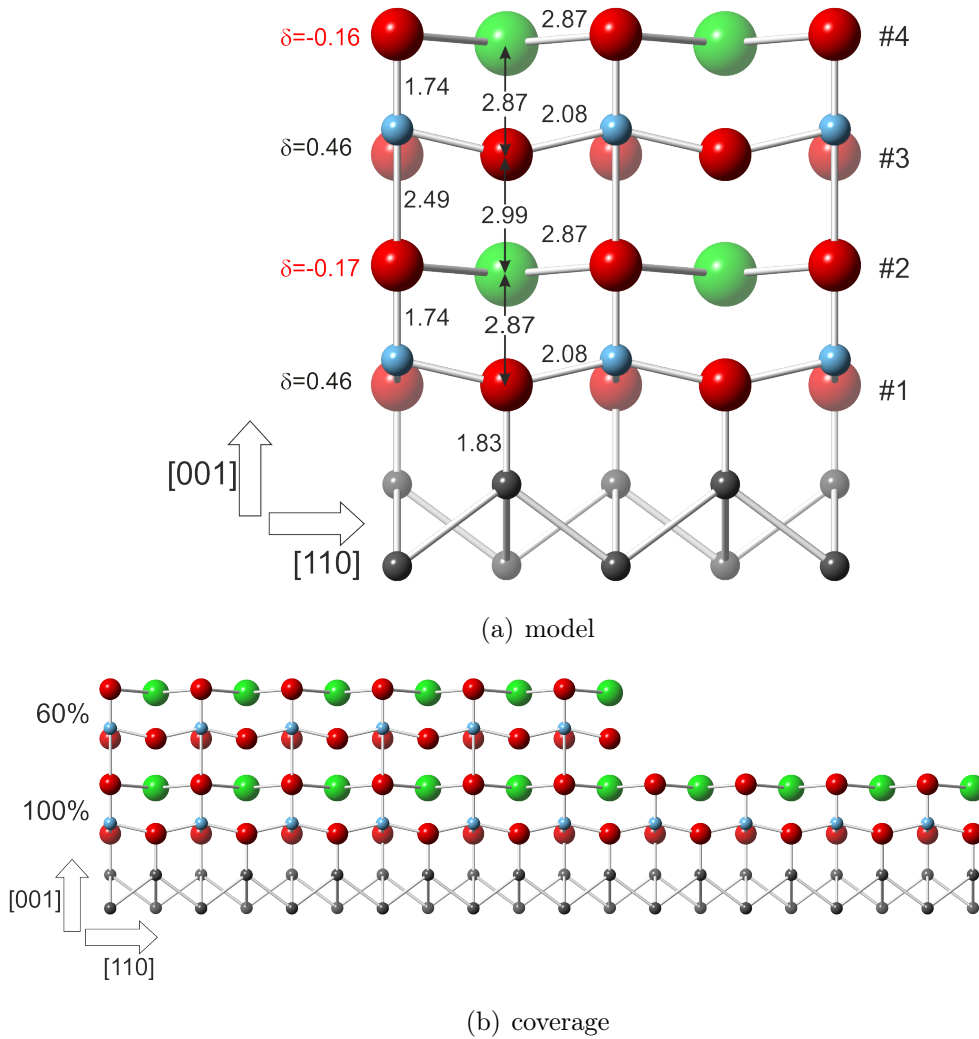**Figure 2.8:** Structure model for the $BaTiO_3(001)$-c(2×2)/Fe(001) sample with a thickness of $1.6\,uc$. All values in Ångström, $\Delta\delta = 0.10\,Å$.

Sample 3Fe

The final Fe(001) sample differs strongly from the other two structure models. Figure 2.9 shows the corresponding structure model and the coverage representation, from which one can see a clear indication of Stranski-Krastanov growth. Basic similarities are the TiO_2-Fe interface with short Fe-O bond length, the BaO top layer with negative δ and growth as full unit cells. There is also the alternating vertical Ti-O bond length with $1.72\,Å$, $2.00\,Å$ and $1.76\,Å$ for the short bond distances and $2.04\,Å$ and $2.45\,Å$ for the long ones.

(a) model

(b) coverage
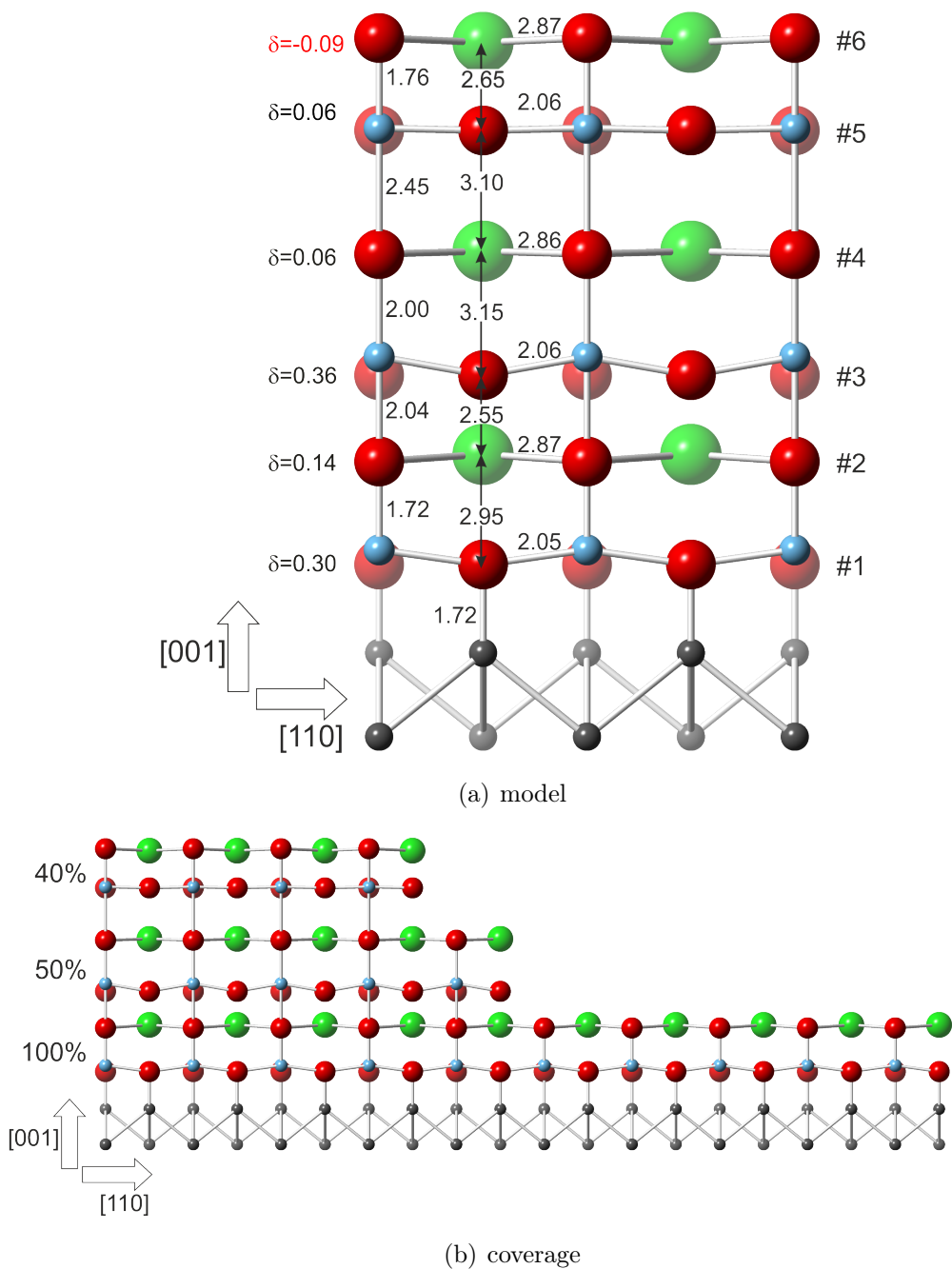
Figure 2.9: Structure model for the $BaTiO_3(001)$-c(2×2)/Fe(001) sample with a thickness of 2.7 uc. All values in Ångström, $\Delta\delta = 0.15 - 0.20$ Å.

The main differences are the non alternating signs of δ and relatively large layer distances on both sides of the second BaO layer. This separates the film in three parts, the first being the substrate interface region (#1-#3) where two layers of TiO_2 and one BaO layer form a close system with all three δ positive

which results in a very short BaO distance of $2.55\,\text{Å}$ between layers #2 and #3. The δ in the BaO layer is about the same size as in sample 2Fe, although the opposite direction and the values for the two TiO_2 layers are about 20% smaller. The second part is the single BaO layer #4 with large distances to the layers on both sides and an almost vanishing positive δ. The last part is the unit cell of $BaTiO_3$ forming the vacuum interface (#5-#6). Here both δ are of opposite sign with the negative BaO shift following the trend of the first two samples and decreasing further to $-0.09 \pm 0.20\,\text{Å}$. The TiO_2 shift is very small with $0.06 \pm 0.20\,\text{Å}$.

With the uncertainty of the position determination being $0.15 - 0.20\,\text{Å}$ the δ for layers 2 and 4-6 are smaller than the error. This means that not only the magnitude but also the sign could in reality be different. This would allow for a structure similar to samples 1Fe and 2Fe, so the data for sample 3Fe is not perfectly conclusive.

STM measurement
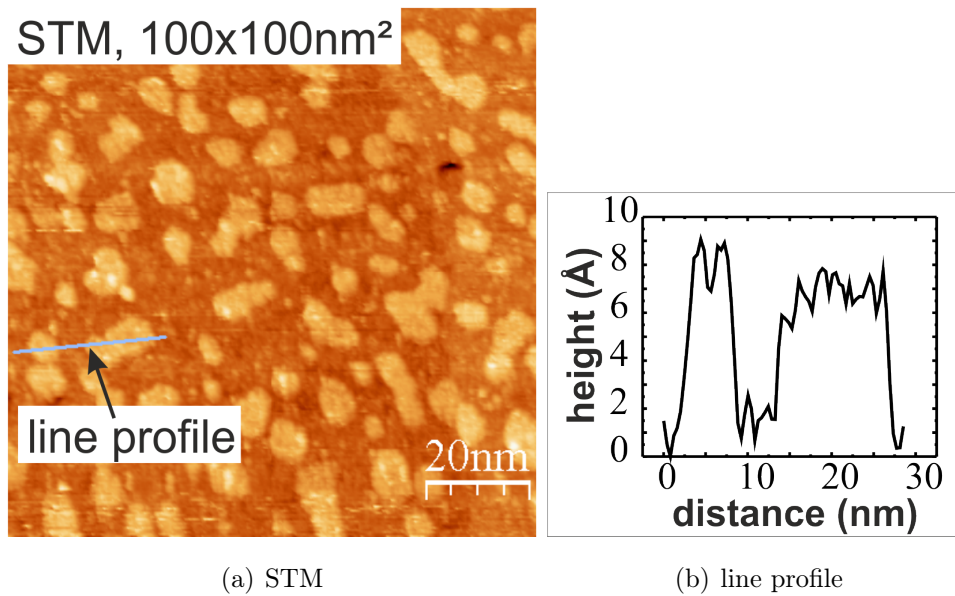
(a) STM   (b) line profile

Figure 2.10: STM image taken from sample with thickness between samples 2Fe and 3Fe showing Stranski-Krastanov growth mode. The right image shows the line profile taken at the position of the gray line in the STM image. It shows steps of multiples of $4\,\text{Å}$, the height of one unit cell of $BaTiO_3$. ($U = +2.25\,\text{V}$, $I = 0.56\,\text{nA}$)

In order to check the surface with a method different from SXRD, STM images have been taken. Figure 2.10 shows one example of a sample with an averaged thickness of about $2\,\text{uc}$. One can see a closed layer of $BaTiO_3$ with a small defect in the upper right quadrant opening to the Fe crystal. On top of this layer many small islands of $BaTiO_3$ of sizes up to $10 - 15\,\text{nm}$ are randomly distributed. These islands have heights of 1, 2 or even 3 unit cells and none have been found differing from these heights. AES measurements and comparison to the SXRD models confirms that the closed layer is $BaTiO_3$ and not the top layer of Fe.

2.1.2 BaTiO$_3$(001)-c(2×2)/Pd(001)
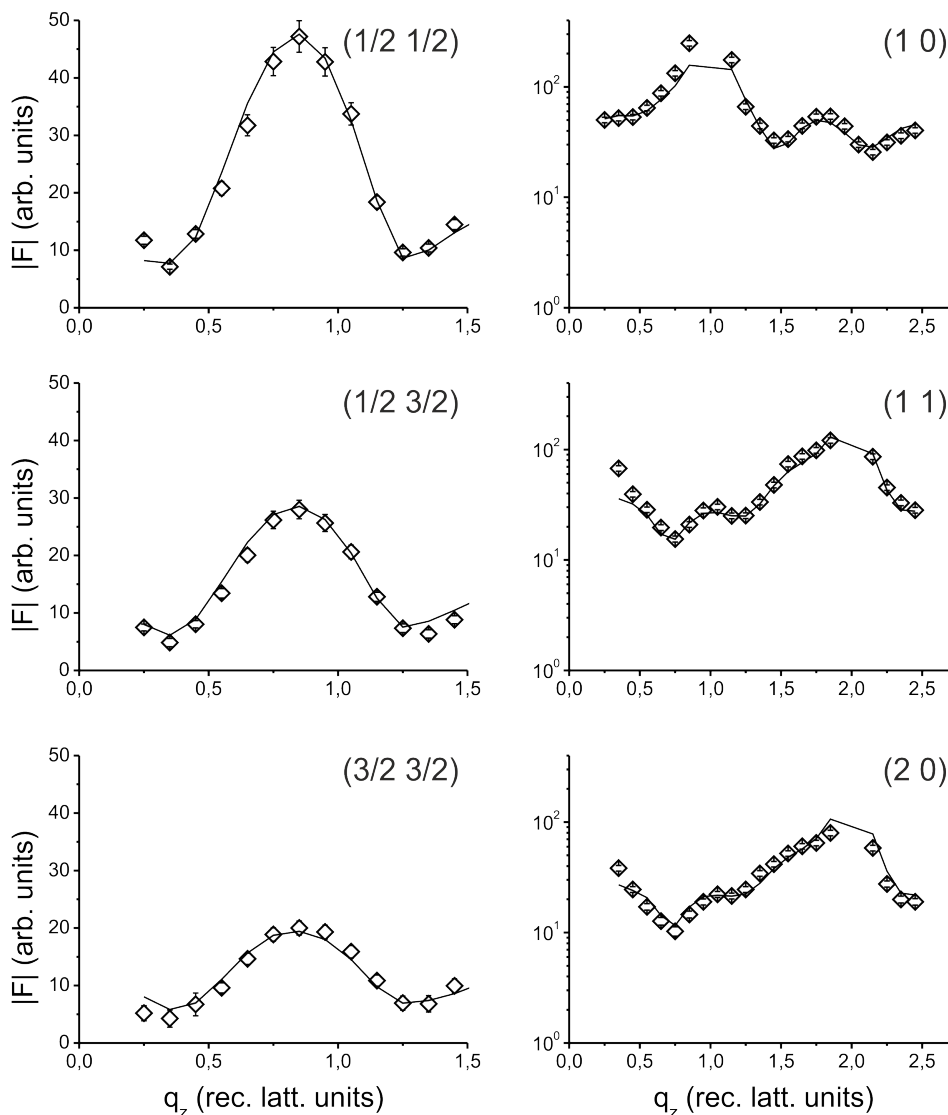
Figure 2.11: Fractional (left, linear scale) and integer order (right, logarithmic scale) rods of the investigated Pd(001) sample. Shown are the measured data points as symbols and the calculated structure factor amplitudes as lines.

Figure 2.12 shows the model of about 1.9 uc BaTiO$_3$ on a Pd(001) crystal. It has many things in common with the Fe models. TiO$_2$ is the interfacial layer and BaO is the topmost layer, but not the only interfacial material towards vacuum (Figure 2.12(b)). There is a large positive vertical shift in the TiO$_2$ layers, a large negative one in the lower BaO layers and the topmost layer has a smaller negative value. The layer separations calculated from the oxygen plane

positions are alternating between larger and smaller, the former between layers #1-#2 and #3-#4 and the latter between layers #2-#3.

(a) model

(b) coverage

Figure 2.12: Structure model for the $BaTiO_3(001)$-$c(2 \times 2)/Pd(001)$ sample with a thickness of 1.9 uc. All values in Ångström, $\Delta\delta = 0.10$ Å.

Different from the Fe samples is that oxygen is incorporated in one of the two possible hollow sites with an occupancy of 50%, situated below the Ba. The Pd-O bond distances of these incorporated oxygen atoms are 1.98 Å in-plane and 2.23 Å out-of-plane being in the same size range as the Pd-O bond distance between substrate and film with 2.30 Å. This is about 0.5 Å larger

than on Fe and is easily explained by the additional oxygen in the substrate top layer leading to a weaker bond between film and substrate. Another difference is the fact, that BaO is not the only interfacial material towards the vacuum. In fact it is the minor contributor to this interface with about 70% being TiO_2. This is coupled with what looks like a change in the overall growth of the film. Contrary to the case on Fe(001), $BaTiO_3$ does not seem to grow on Pd(001) as full unit cells, but with a closed layer of TiO_2 at the interface and a partially occupied unit cell layer of $BaTiO_3$. On top of this is a small amount of BaO.

## 2.1.3   BaTiO$_3$(001)-c(2×2)/Pt(001)
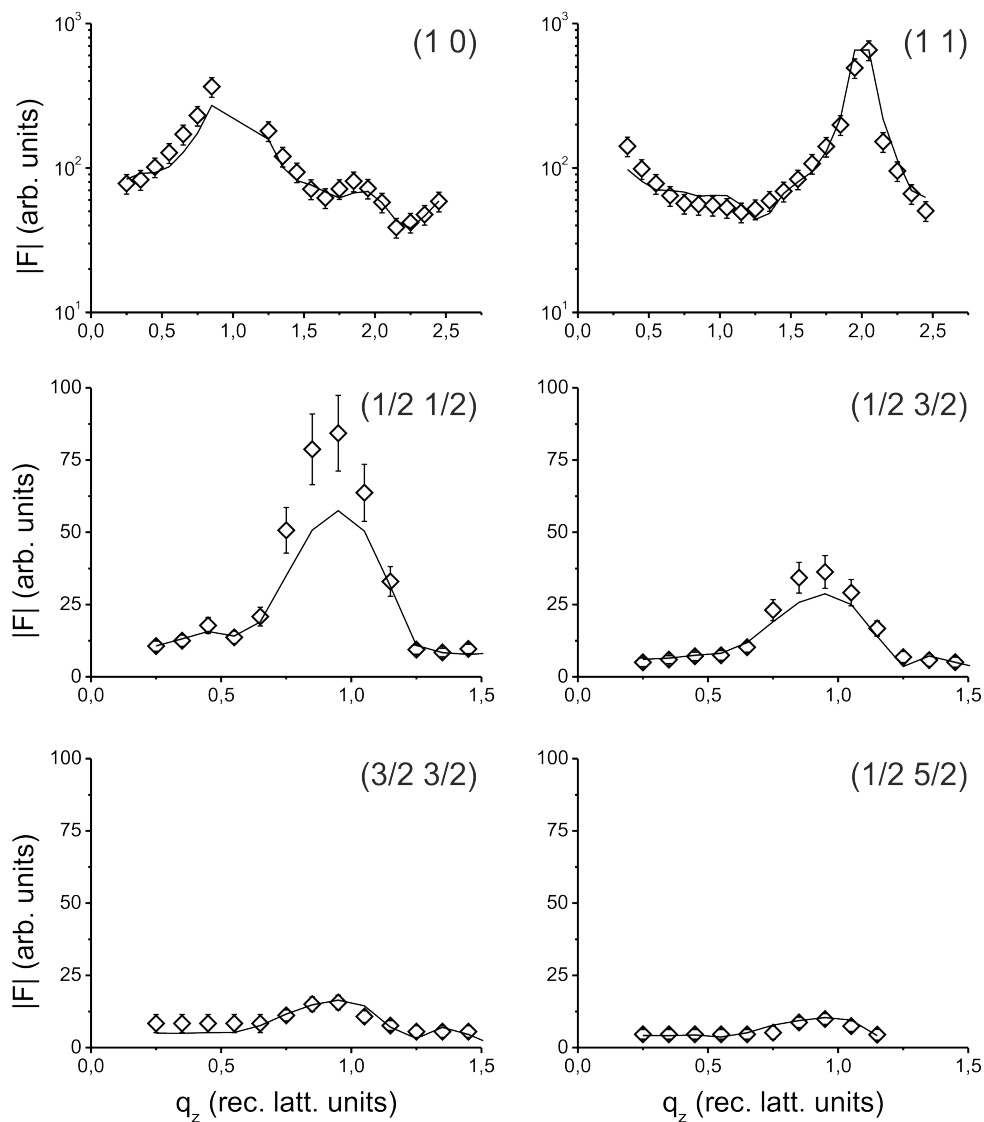
Figure 2.13: Fractional (bottom two rows, linear scale) and integer order (top row, logarithmic scale) rods of the investigated Pt(001) sample. Shown are the measured data points as symbols and the calculated structure factor amplitudes as lines.

For the Pt sample with c(2 × 2) reconstruction a single domain phase has not been achieved, only a phase with 3 c(2 × 2) domains rotated by 30° to one another. For this work only the most prominent in intensity has been investigated. The structure is outlined in Figure 2.14 which shows TiO$_2$ being the interfacial layer towards both, Fe and vacuum. In Figure 2.14(b) it is visible, that TiO$_2$ forms the whole BaTiO$_3$-vacuum interface and no BaO top

layer is present.

(a) model

(b) coverage

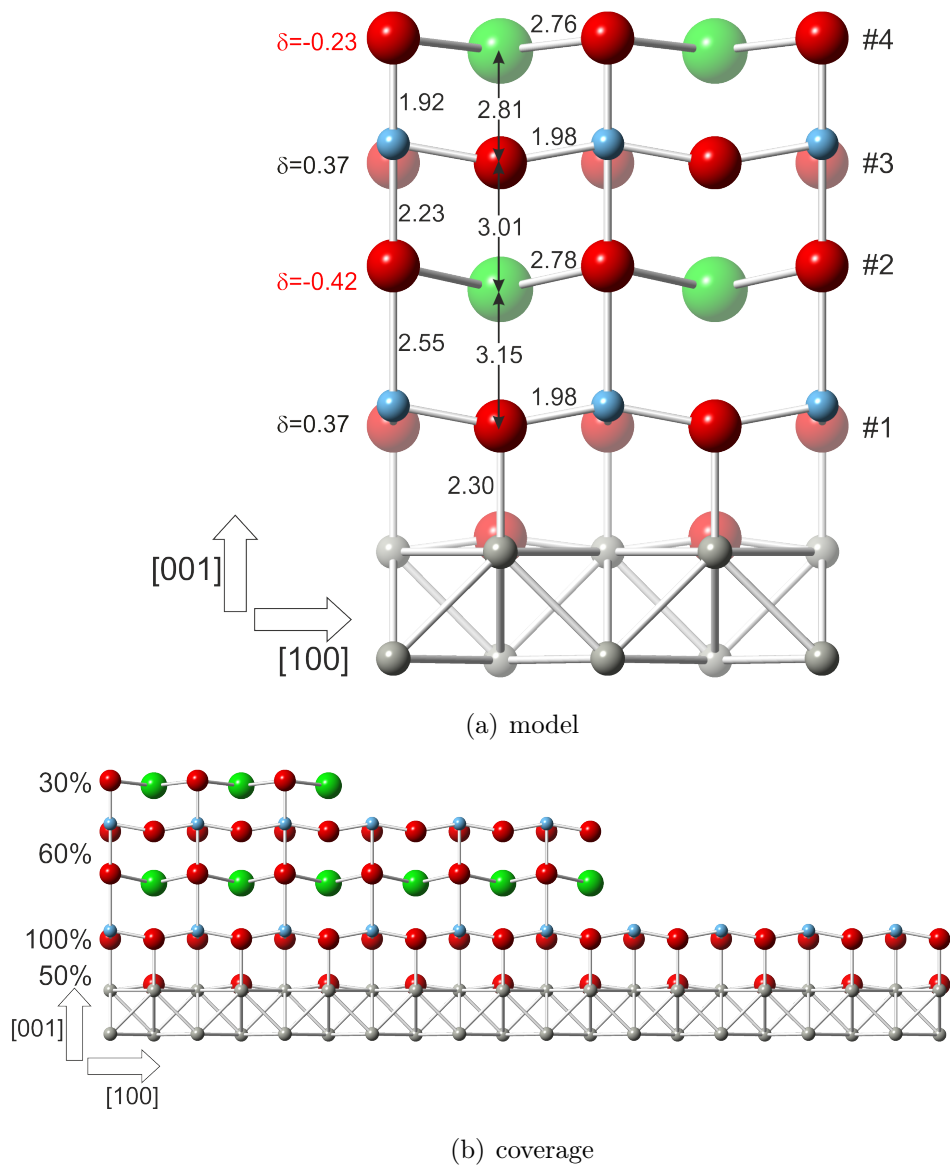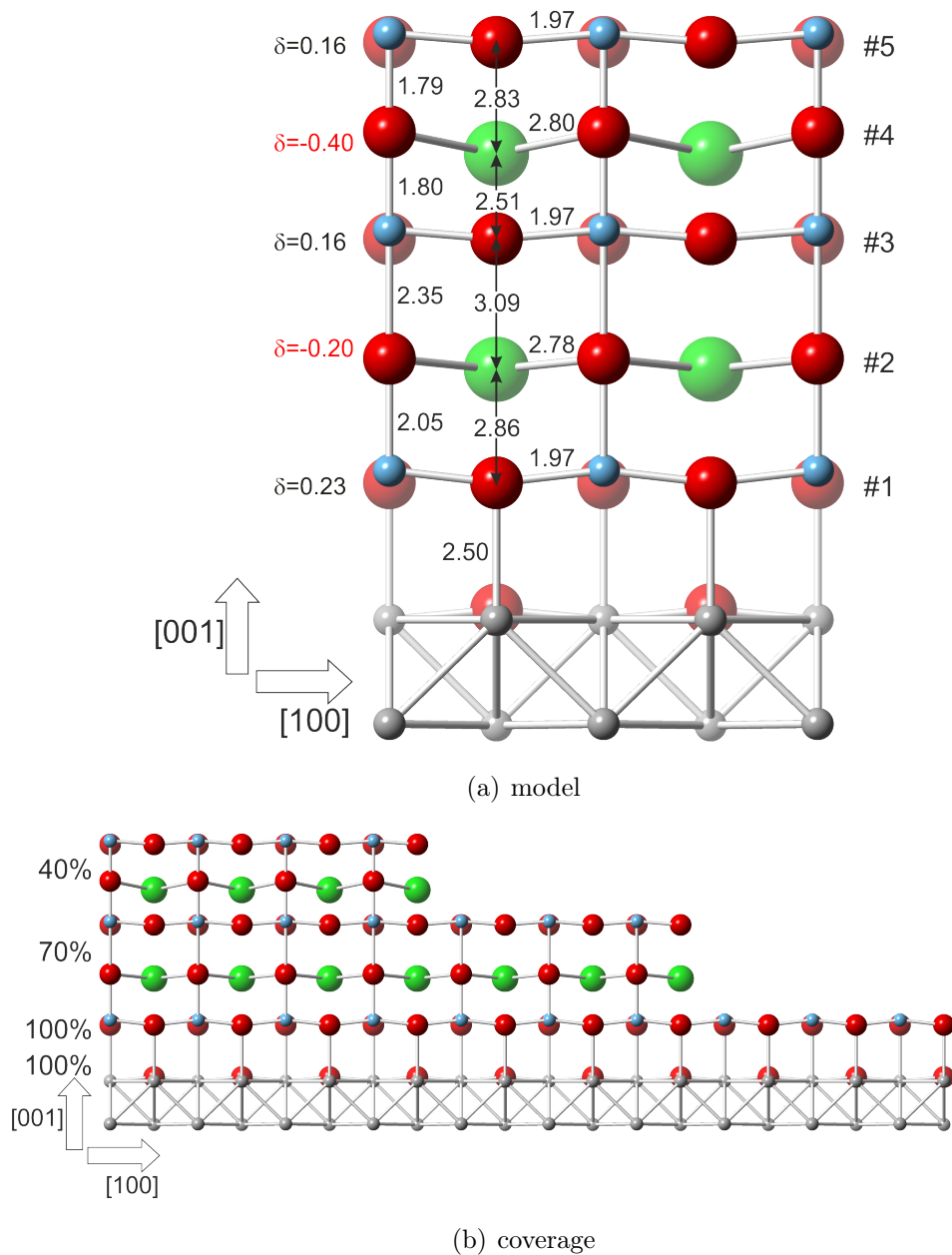**Figure 2.14:** Structure model for the $BaTiO_3(001)$-$c(2\times2)$/$Pt(001)$ sample with a thickness of $2.1\,uc$. All values in Ångström, $\Delta\delta = 0.10\,\text{Å}$.

Like in the previous model the vertical shift of the BaO layers is relatively large and negative and that of the TiO_2 layers is smaller and positive. Also continuing the phenomenon of changed growth behavior from the Pd sample, the film on Pt grows by creating a closed layer of TiO_2 and then growing unit cell layers of $BaTiO_3$ above this interfacial layer. These two unit cell

layers show different bond distances with longer ones around 2.3 Å for the first TiO_2-BaO-TiO_2 trilayer (#1-#3) and shorter ones with less than 2.00 Å for the upper trilayer (#3-#5).

The hollow site of the Pt surface below the Ba atom is similar to Pd(001) filled with oxygen but with 100% occupancy. The bond lengths from Pt to this oxygen are comparably short with 1.97 Å in-plane and 2.11 Å out-of-plane and the Pd-O distance towards the film is distinctively longer with 2.5 Å.

2.1.4   Discussion

Concluding the experiments of ultrathin $BaTiO_3$ films on metal single crystals one can summarize that Barium Titanate grows on all three investigated substrates in a well ordered c(2×2) reconstruction and all samples show significant vertical shift of the ionic species relative to each other. Figure 2.15 shows the δ values in the film layers of the three Fe(001) samples. Sample 1Fe with only one unit cell of $BaTiO_3$ (black) shows no shift in the TiO_2 layer leading to no spontaneous electric polarization. Starting with 2 unit cells of $BaTiO_3$ (red) a strong vertical shift in all TiO_2 layers indicates the presence of a strong electric polarizaion which is also present in the thickest investigated sample 3Fe (blue). The onset of polarization with two layers of $BaTiO_3$ confirms theoretical predictions for a lower limit of ferroelectricity in perovskite oxides.[49]

Also visible in the diagram is that the terminating BaO layer in all the samples has a negative vertical shift, not only on Fe(001) but also on the Pd(001) crystal although it is only partially BaO terminated. This has been investigated theoretically and is shown in Figure 2.16 for sample 1Fe.[47] These calculations show, that an unrelaxed BaO termination layer has a polarized surface which can be neutralized by an inward relaxation of the Barium atoms leading to a flat isocharge surface.

In addition to this, first-principle calculations of the $BaTiO_3$/Fe(001) interface were carried out and confirmed that the TiO_2/Fe(001) interface is energetically more favorable than the BaO/Fe(001) interface by approximately 2 eV per unit cell. The Oxygen sits on the top sites and forms very strong chemical bonds with the surface Iron atoms leading to the very short bond distances of about 1.8 Å. This is in very good agreement with the proposed model, the

earlier mentioned calculations by Fechner *et al.*[48] and work done by Duan *et al.*[5] For the BaO/Fe(001) interface the calculations show unrealistically large distances between substrate and film and thus it was excluded from the data analysis.[50]
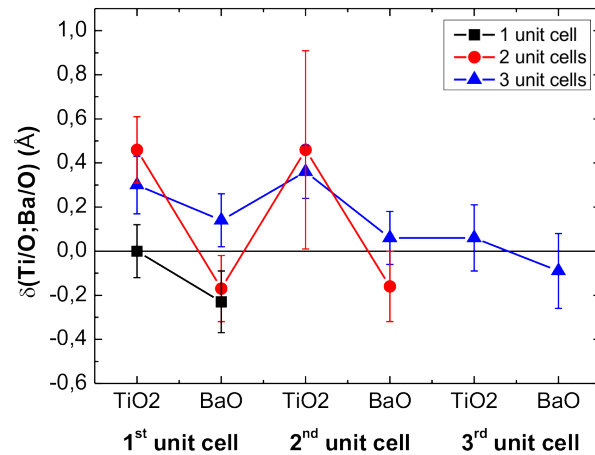
Figure 2.15: Diagram depicting the vertical shift δ of the different layers for three BaTiO$_3$ coverages on Fe(001)
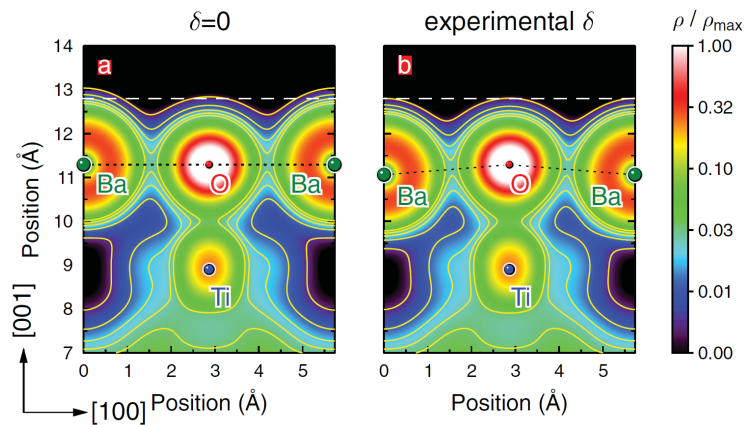
Figure 2.16: Calculated charge density of one unit cell of BaTiO$_3$ on a Fe(001) crystal. Comparison of unrelaxed positions (left) with the experimentally obtained value $\delta = -0.23\,\text{Å}$ (right) shows a flat isocharge surface for the relaxed case.[47]

Part of these calculations was the study of the behavior of single Oxygen atoms when they are placed on the clean metal surface. On Fe(001) all the Oxygen atoms prefer the on-top site of the surface supporting the stability of

the TiO_2/Fe(001) interface. For Pd(001) and Pt(001) only part of the Oxygen positions on-top of the metal and the rest prefers the hollow sites, which explains the integration of Oxygen into these surfaces below the $BaTiO_3$ and their increased metal-Oxygen bond distances between the film and substrate.[50]

In order to investigate the multiferroic properties of the interface a third set of calculations was performed. Figure 2.17 shows a compilation of these results. The blue lines show the δ values for the separate layers with the solid triangles ($P_\uparrow$) showing the model proposed for sample 3Fe. The switched polarization ($P_\downarrow$) is marked with the empty squares and simulated by changing the sign of all δ except the uppermost BaO layer in order to preserve the surface charge neutrality. The red lines are the calculated magnetic moments for both polarization directions and one can see that they do not differ significantly except for the interfacial Titanium. Here there is a strong change from $m_{Ti1} = 0.03\,\mu_B$ to $m_{Ti1} = -0.35\,\mu_B$ switching from $P_\uparrow$ to $P_\downarrow$, resulting in ferromagnetic and antiferromagnetic coupling states, respectively. The effect on the interfacial Iron is comparably small changing from $m_{Fe1} = 2.59\,\mu_B$ to $m_{Fe1} = 2.56\,\mu_B$.

Figure 2.17: Vertical displacements δ (blue) and layer resolved magnetic moments (red) for $P_\uparrow$ (triangles) and $P_\downarrow$ (squares) for sample 3Fe. The inset shows the total energy change (ΔE). [47]

The inset in Figure 2.17 shows the total energy change (ΔE) for the three cases of $P_\uparrow$, $P_\downarrow$ and $P = 0$ indicate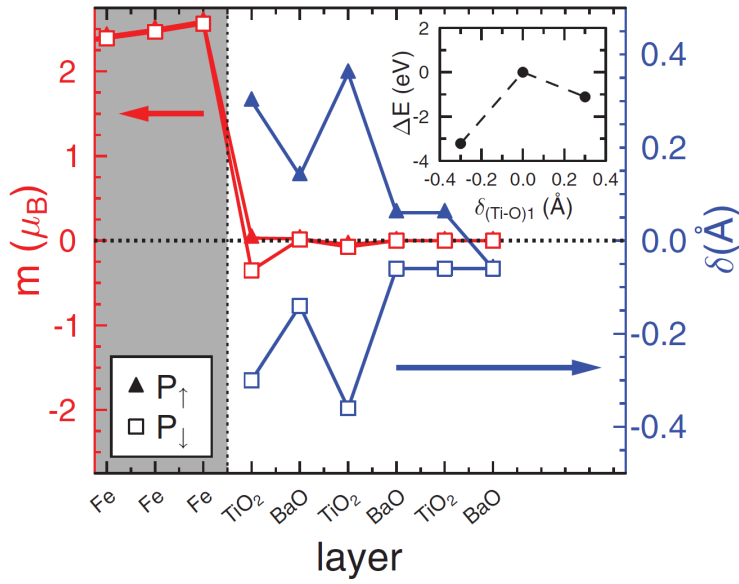d by the corresponding values of $\delta_{(Ti-O1)}$. It is clearly visible, that the present model for $P_\uparrow$ has lower energy than the unpolarized state and that the opposite polarization $P_\downarrow$ is even lower by about $2\,\mathrm{eV}$. Since the unpolarized state in this calculation acts as a saddle point permanent switching seems possible.

The growth of $BaTiO_3$ on Pd(001) and Pt(001) shows a very different behavior to the Fe(001) crystal where the $BaTiO_3$ always grows in unit cell thick layers. This happens to create a charge neutrality for the film which is achieved in the BaO/TiO_2 bilayer. Preliminary calculations show that the integration of Oxygen into the substrate surface leads to charge neutrality for the TiO_2/metal interface which results in unit cell growth starting with the first BaO layer and not already at the interface TiO_2.[50] This forces parts of the film to a TiO_2 termination in order to create charge neutrality. For the Pd(001) substrate the integration of Oxygen into the surface is not complete and only partial TiO_2 coverage is the result. The Pt(001) sample has a higher percentage of Oxygen present in the metal surface and the TiO_2 termination is at 100 %. The Oxygen dependent change in these systems is not fully explained as of now and the investigations are still ongoing.[50]

Also considering the Palladium and Platinum crystals the earlier calculations regarding the δ values hold true for the BaO terminated part of the sample. For the TiO_2 terminated part the shift is positive and calculations about this termination are as of the writing of this work not yet completed.

Another aspect is the Ti-O bond length dependence upon the lattice constant as shown in Figure 1.3. Here one can see an increase in the vertical shift of the Titanium atom with increasing lattice constant. Comparing these calculations to the structural models was done by defining layers $2 - 4$ for all samples and additionally layers $4 - 6$ for sample 3Fe as the $BaO/TiO_2/BaO$ cell used for the calculations. Since sample 1Fe does not contain layers 3 and 4 it will not be used in this comparison. Table 2.1 lists all the necessary data. For every sample the in-plane (a) and out-of-plane (c) lattice constants as well as $\frac{c}{a}$ are included. These values are necessary to extract the bond distances d^{calc} from Figure 1.3.

One can see, that the $\frac{c}{a}$-value for all stacks differs by less than 7% from the

Sample, layer	a	c	c/a	d_S^{exp}	d_S^{calc}	d_L^{exp}	d_L^{calc}
2Fe, 2-4	4.05	4.23	1.0444	1.74	1.77	2.49	2.46
3Fe, 2-4	4.05	4.04	0.9975	2.00	1.83	2.04	2.22
3Fe, 4-6	4.05	4.21	1.0395	1.76	1.76	2.45	2.45
Pd, 2-4	3.89	4.15	1.0668	1.92	1.80	2.23	2.35
Pt, 2-4	3.92	4.15	1.0587	1.80	1.80	2.35	2.35

Table 2.1: Vertical Ti-O bond distances gathered from the experiment (d^{exp}) compared to the calculations in Figure 1.3 (d^{calc}). Indices S and L denote the short and long bond, respectively. Also listed are the lattice constants a and c for the investigated layers used to gather the lengths from the diagram.

values used in the calculations (1.013 and 1.0067) and since these calculations have shown no depencene upon $\frac{c}{a}$, the already calculated bond lengths are assumed to be similar to those with the exact $\frac{c}{a}$-value. Comparing the d^{exp} and d^{calc} values shows that for samples 2Fe, Pt and layers 4-6 of sample 3Fe the agreement is very good and the Pd sample differs by less than 7%. For layers 2-4 of sample 3Fe the difference is already 10% and the short and long bond length are almost identical which in agreement with the corresponding lattice constants a and c indicates a more cubic behavior in contrast to the tetragonal behavior of the other samples. Opposing this is the large vertical shift in layer 3 being distinctively different from the cubic crystal in which the δ is 0.00 Å for every layer. This leads to the conclusion, that for the thicker sample additional experiments should be performed with the hope of increasing the coverage of the existing layers of the film without increasing the number of layers present. This would help with increasing the quality of the analysis even further by increasing the measured signal for these layers and thus improve the signal-to-background ratio.

2.2 Fe on the surface of BaTiO$_3$ thin films and single crystals

Theoretical works like Duan *et al.*[5] cover the properties of BaTiO$_3$/Fe multilayers with the Barium Titanate interfacing with Iron on both sides. Since

this is the logical extension of the first part of this work, experiments have been performed to reproduce these structures by depositing Iron on top of a $BaTiO_3$-c(2×2)/Fe(001) structure. Fe(001) samples with varying $BaTiO_3$ thicknesses were used as substrates for thermal deposition of Iron. AES plots show a significant increase in Fe after deposition and LEED images show a (1×1) structure of Fe(001) with decreased clarity. Figure 2.18 shows the (1 0 L) rod of Fe on $4.5\,uc$ $BaTiO_3$(001)-c(2×2)/Fe(001). The image shows, representative for all performed measurements, that inside the measurement errors no discernible difference between the data with and without additional Fe could be found. This leads to the conclusion that for the used samples the grown Fe layer is disordered.
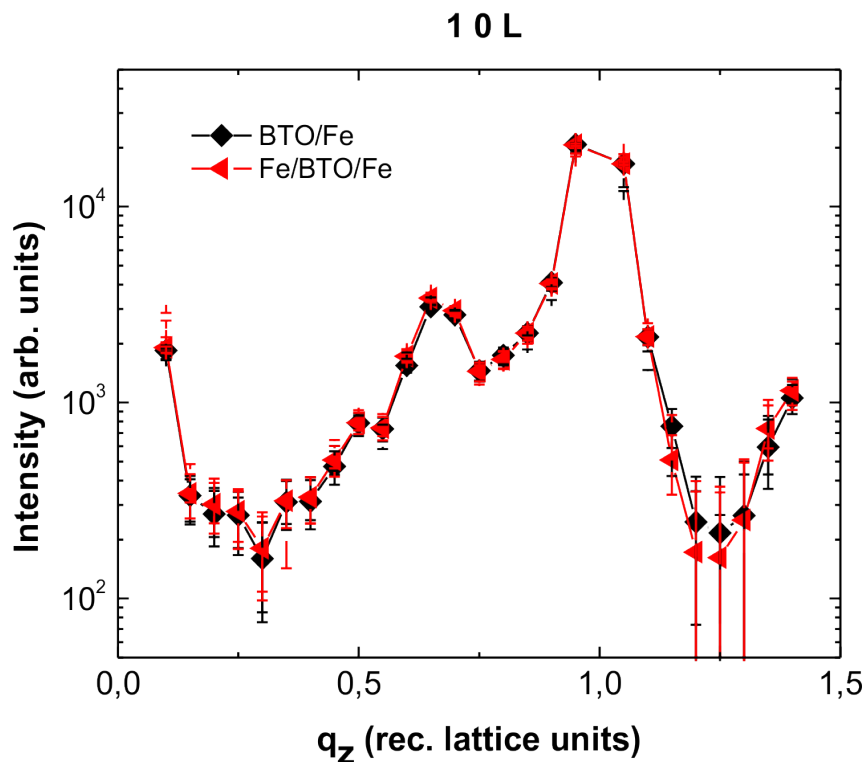
Figure 2.18: Comparison of measured structure factors for $BaTiO_3$-c(2×2)/Fe(001) with and without additional Fe are shown for the (1 0 L) rod in red and black, respectively.

The reasons for the failure to grow an ordered layer of Fe is not known yet, but to investigate if the Fe might have diffused through the $BaTiO_3$ towards the Fe(001) crystal another measurement has been performed on a single crystal of $BaTiO_3$(001). Figure 2.19 shows the measured structure factors for two rods of

the sample before and after the deposition of Fe. Again there is no difference between the two datasets visible.
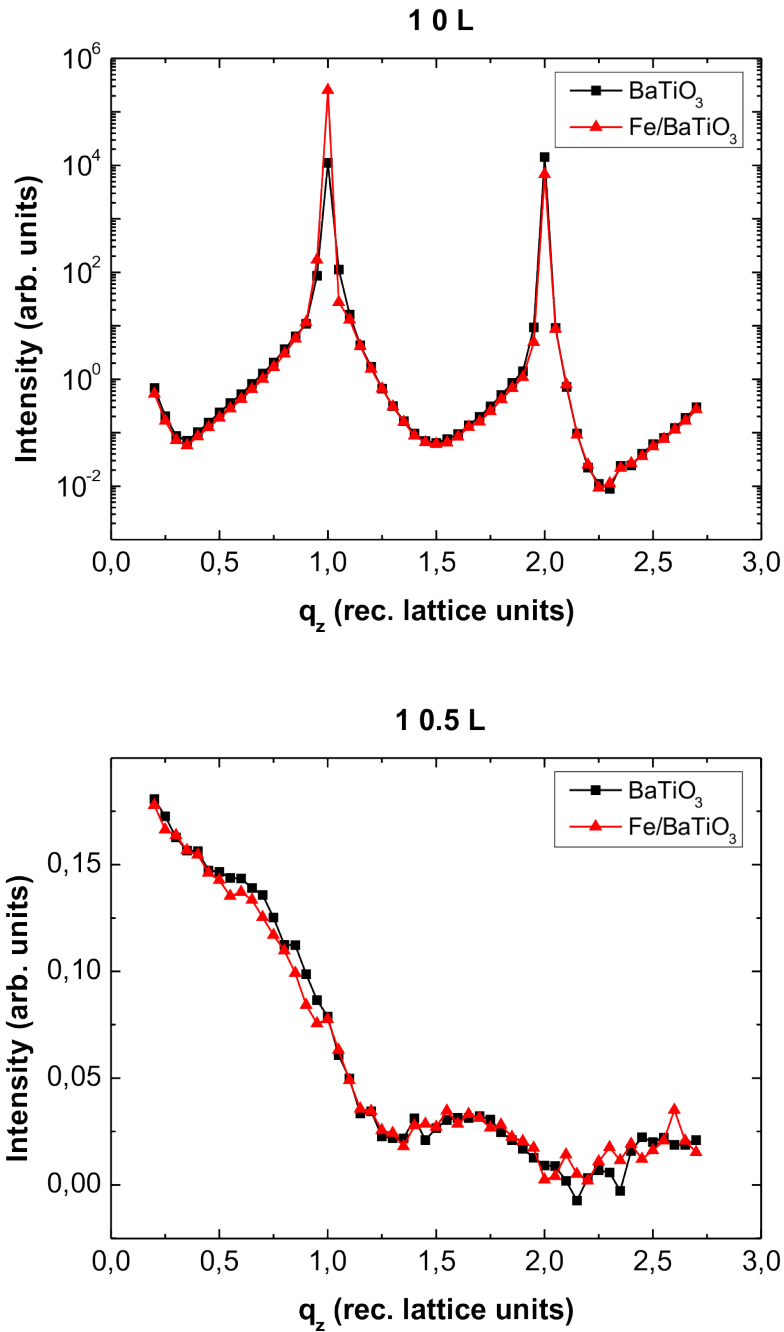
Figure 2.19: Measured structure factors for the Fe/BaTiO$_3$(001)-c(2 × 1) sample for the (1 0 L) CTR and the the (1 0.5 L) SLR.

These two experiments lead to the conclusion, that the structure theoreti-

cally investigated by Duan *et al.*[5] could not be reproduced with the present series of experiments. This does not disprove the theory but it provides information, that the creation of such a system requires different procedures and more research. One possible direction of research would be to follow the work by Meyerheim *et al.* and Tusche *et al.* on the Fe/MgO/Fe(001) system.[51–54] They could not grow a well ordered Fe layer on top of an MgO film and related it to the surface free energies of the two materials with $2.9 \frac{J}{m^2}$ and $1.1 \frac{J}{m^2}$ for Fe and MgO, respectively.[55, 56] These energies resulted in well ordered growth of MgO on Fe but not vice versa. On closer inspection an FeO layer formed on top of the Fe(001) crystal as an interface between MgO and Fe which lead to the idea of Oxygen assisted growth of Fe on MgO. This in turn resulted in an ordered growth of an Fe/MgO/Fe(001) system.

Analogous conclusions can be drawn from the fact that the free surface energy of $BaTiO_3$ is in the same range as that of MgO with $1.0 - 1.2 \frac{J}{m^2}$.[57] Thus a well ordered layer might be formed by Oxygen assisted growth of Fe but no FeO interface layer has been found on any of the $BaTiO_3$/Fe(001) samples and the BaO termination is not favorable for the growth of Fe as confirmed by theory. Considering the results for the Pd(001) and Pt(001) crystals in the previous section, these substrates might be better candidates for the pure growth of a sandwhich like structure because incorporation of Oxygen into the interface and TiO_2 termination of the film has been found on these crystals.

2.3 Investigation of the p(2×1) reconstructed surface of a $BaTiO_3$ single crystal

The (2×1) reconstructed surface of $BaTiO_3$ is already known for more than 30 years[58] and many other reconstructions have also been reported [(1×1), (2×1), c(2×2), p(2×2), $(\sqrt{5} \times \sqrt{5})$, (3×1), (3×2) and (6×1)][59–64] but no experimental study has been performed yet to determine the atomic structure of this reconstruction. Only for the paraelectric Strontium Titanate $(SrTiO_3)$ does a quantitative experimental investigation of the (2×1) surface structure exist (combined with a p(2×2) reconstruction).[65–67] This chapter will provide information about such a study on the $BaTiO_3(001)$-(2×1) surface and detail a model (shown in Figure 2.20).[43]
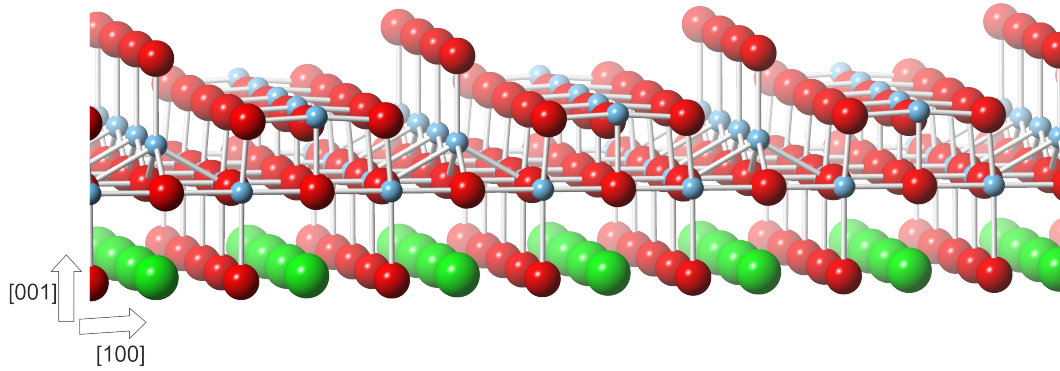
Figure 2.20: (2×1) surface reconstruction of an annealed $BaTiO_3$ bulk crystal showing the termination by a TiO_2 double layer. Green, blue and red spheres correspond to Barium, Titanium and Oxygen, respectively.

To achieve a (2×1) reconstruction the polished $BaTiO_3$ crystal ($\oslash = 5$ mm, $d = 3$ mm from Mateck GmbH (Germany)) has been sputtered with Ar+ ions (1 keV, 3×10^{-5} mbar) for 30 minutes and annealed for 40 minutes to $1100 - 1200$ K in a UHV chamber with a base pressure in the 10^{-10} mbar range at the beamline ID03 of the ESRF. This treatment leads to a two domain (2×1) reconstruction as shown in Figure 2.21 with no indication of p(2×2), clearly differing from the data gathered by Herger *et al.*[66, 67] AES measurements did not show any contamination of the surface.
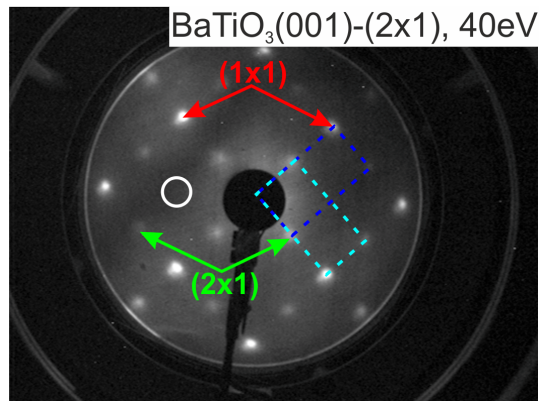
Figure 2.21: LEED image of the (2×1) reconstructed surface of a $BaTiO_3(001)$ single crystal annealed at 1100 K. The red and green arrows point to LEED spots corresponding to the (1×1) and p(2×1) structure, respectively. The light and dark blue boxes outline the two rotated p(2×1) domains and the white circle marks the area where an additional spot would appear, if the p(2×2) reconstruction would be present.

Preliminary STM measurements were performed and an image with a height

profile is displayed in Figure 2.22. The image shows terraces of $30-70\,\text{nm}$ width and a uniform step height of $4\,\text{Å}$, corresponding to a uniform termination.
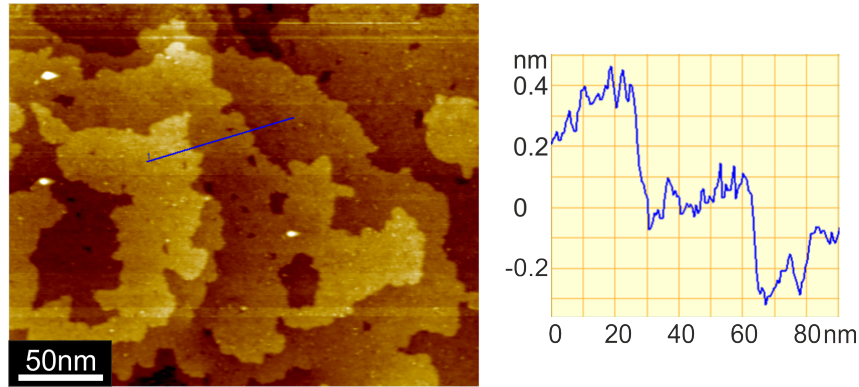
Figure 2.22: STM image of the (2×1) reconstructed surface of a $BaTiO_3(001)$ single crystal annealed at $1100\,\text{K}$. The marked height profile shows unit cell high steps and thus a uniform termination. $(U = +2.0\,\text{V}, I = 1.0\,\text{nA})$

X-ray diffraction reflection intensities were collected with a pixel detector using grazing incidence $(\alpha_i = 2°)$ of the incoming beam $(\lambda = 0.69\,\text{Å})$. The data consisted of 16 fractional and 8 integer order rods between $l = 0.2$ and $l = 2.8$ reciprocal lattice units (r.l.u.). These were averaged over symmetry equivalent reflections and corrected for instrumental factors. For the first investigation the fractional order in-plane reflection intensities $I(hkl)$ with $l = 0.2\,\text{r.l.u.}$ were used which are tabulated in Figure 2.23 along with some examples of the measured (symbols) and calculated (lines) structure factor amplitudes.

The $l = 0.2\,\text{r.l.u.}$ intensities were used to calculate the z-projected Patterson function by setting the l value to 0, which is a good enough approximation for a qualitative analysis. The Patterson function is displayed in Figure 2.24(a) and all maxima are labelled with letters from **A** to **F**. Peak **A** is the trivial peak corresponding to the self correlation of all the atoms in the unit cell, this peak is present in all Patterson functions. Peaks **B**, **C** and **D** are intense maxima describing correlations to reconstructed atoms for the former and vacancies for the latter two. The less intense maxima **E** and **F** with positive and negative contributions can be attributed to an atom shifting from its bulk position towards the positive maxima.
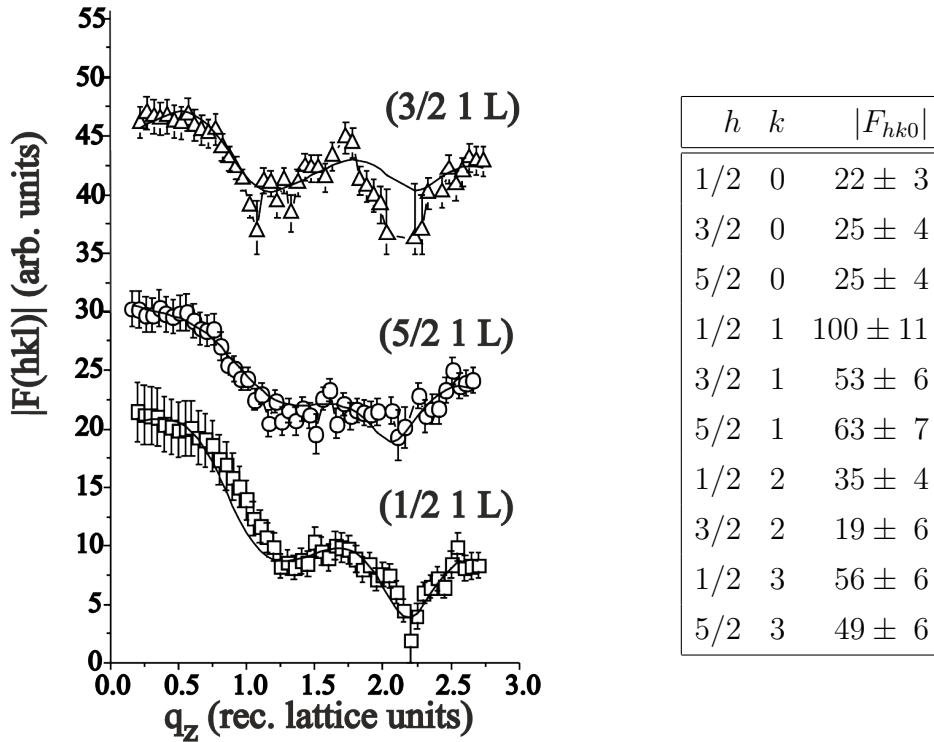
Figure 2.23: Structure factor amplitudes as measured by SXRD (symbols) and calculated (lines) with curves shifted vertically for clarity. The table lists the normalized in-plane structure factor amplitudes and their standard deviations.[43]

(a) Patterson map

(b) Plane group $p2mm$
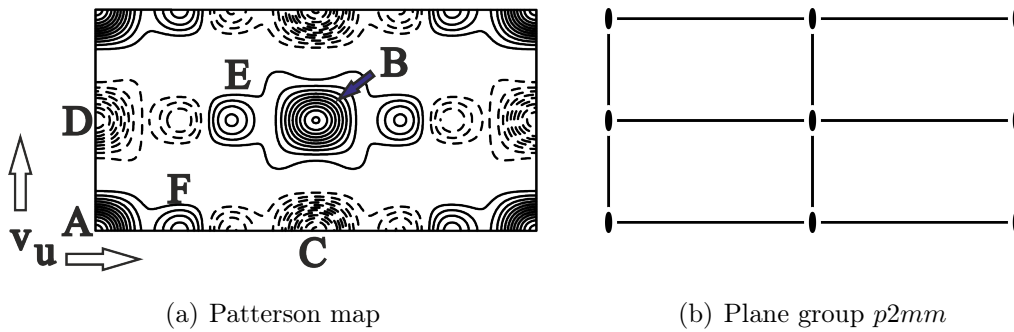
Figure 2.24: a) Contour map calculated using the Patterson function. Solid and dashed lines depict positive and negative maxima, respectively, which define vectors pointing from one atom to either another atom or a vacancy, both of which are not present in the unreconstructed surface. Maxima are labeled with A to F[43]. b) Diagram depicting plane group $p2mm$.[44] This symmetry is used for the analysis.

The information gathered by the Patterson function in combination with a double layer TiO_2 termination found for the surface of $SrTiO_3$[65–67] is a good starting point for the analysis of the whole dataset measured. The final

structural model is presented in Figure 2.25 with the before mentioned double layer TiO_2 termination. These two layers are the ones taking part in the (2×1) reconstruction with the inner one only showing small relaxations. Movements described in the text below are mirrored by similar atoms according to the $p2mm$ plane group symmetry.[44]
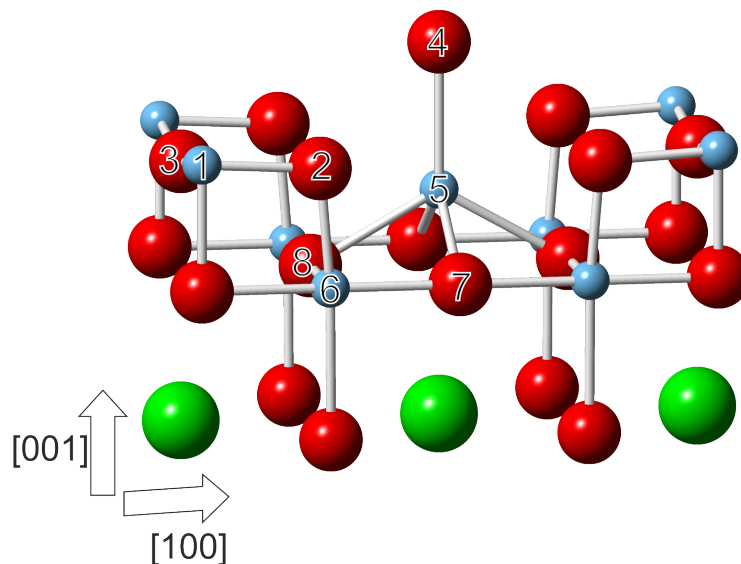
Figure 2.25: Unit cell of the (2×1) reconstruction of an annealed $BaTiO_3$ bulk surface which is terminated by a TiO_2 double layer. Atoms are numbered for clarification.

Figure 2.26 shows the structure model in comparison to an unreconstructed $BaTiO_3$ surface which is terminated by two TiO_2 layers. The unreconstructed structure is depicted by grey atoms where Oxygen is the larger and Titanium the smaller one, not accounting for vertical expansion for simplicity's sake.

In the model a Titanium atom from $(\frac{1}{2}, 0)$ shifts to the center of the (2×1) unit cell at $(\frac{1}{2}, \frac{1}{2})$ (atom #5) and moves into the gap of the second TiO_2 layer with the nearest Oxygen atoms being at a distance of $2.29 \pm 0.15\,\text{Å}$ (bonds #5-#7 and #5-#8). The Oxygen at the $(\frac{1}{2}, \frac{1}{2})$ position (#4) moves up forming a bond distance of $2.30 \pm 0.15\,\text{Å}$ to the shifted Titanium directly below (#4-#5). This movement can be attributed to the **B** peak in the Patterson function in such a way, that this peak describes the correlation between the Titanium at the unit cell origin (#1) and the Titanium atom now in the center of the cell (#5).
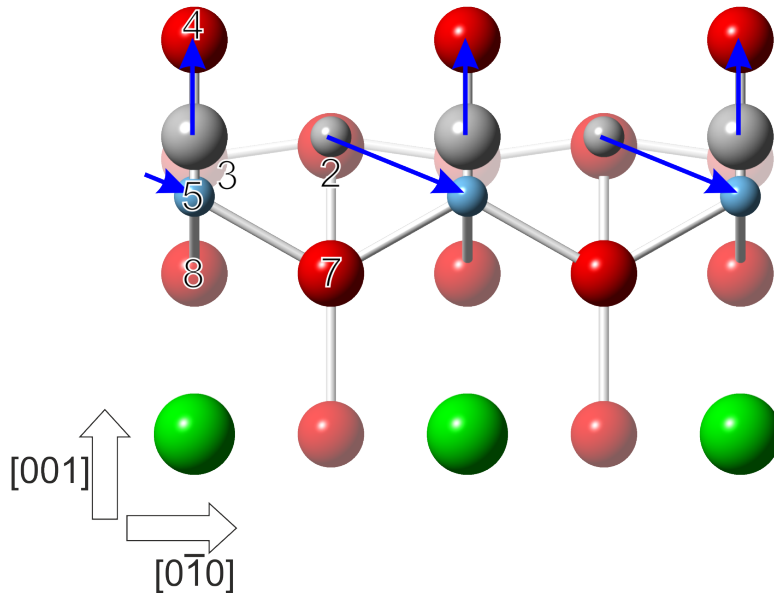
(a) side view
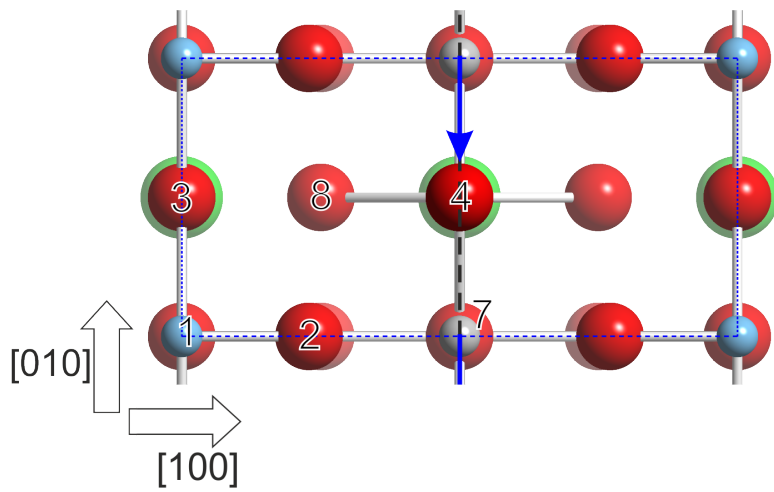
(b) top view

Figure 2.26: Changes in the $BaTiO_3$-(2×1) surface structure compared to a $BaTiO_3$-(1×1) surface (visualized by the grey atoms, with Oxygen and Titanium being the larger and smaller one, respectively), terminated by a TiO_2 double layer. a) Side view of the reconstruction with the distance between the two TiO_2 layers in the (1×1) case set to $BaTiO_3$ bulk layer spacing of approximately $2\,\text{Å}$. Clearly visible is the drop of the Titanium atom (#5) and the floating of Oxygen (#4) b) Top view with the dashed blue line marking the unit cell [(1×1) Oxygen not visible below its (2×1) counterpart].

This also explains the negative peaks at **C** and **D** with the correlation between the reconstruction vacancy and the #5 and #1 Titanium, respectively. The smaller peaks at **E** and **F** are connected to relaxations following the relocation of the Titanium atom. **E** results from a slight movement from Oxygen atom #8 towards the unit cell center ($\approx 0.05 - 0.10$ Å) and **F** from horizontal movements from atoms #2 (Oxygen) and #6 (Titanium) towards Titanium atom #1. Further relaxation not visible with the Patterson function occurs for Oxygen atoms #2 and #3 which relax inward relative to Titanium #1 by 0.1 Å and 0.3 Å, respectively and additionally the layer to layer distance between BaO and TiO_2 expands by about 5%. Atomic bond lengths for all atoms in this model are listed in Table 2.2.

Atoms	Bond length
1-2	1.82± 0.15
1-3	2.01± 0.15
2-6	1.88± 0.15
8-6	2.00± 0.15
5-4	2.30± 0.15
5-8	2.29± 0.15
7-6	2.01± 0.15
Ba-O (in-plane)	2.82± 0.15
Ba-O (out-of-plane)	3.09± 0.15

Table 2.2: Atomic bond distances for the structural model for the $BaTiO_3$(001)-p(2×2) reconstruction

This model leads to $R_u = 10\%$ (Equation 1.16) and thus is of very good quality. If for example Oxygen #4 is removed the value almost doubles to $R_u = 19\%$ indicating the importance of this atoms position. Other models like the pm-(2×1) structure proposed for $SrTiO_3$[65–67] have also been considered but, yielding $30\% \leq R_u \leq 45\%$, have been deemed unsatisfactory.

After analysis, *ab initio* calculations were performed to compare the stability of the resulting p(2×1) structure with the Titanium atom at position ($\frac{1}{2}$, $\frac{1}{2}$) (#5) to the (1×1) [Ti at position ($\frac{1}{2}$, 0) above atom #7] and the (2×1) structure proposed for $SrTiO_3$ by Herger *et al.*[66, 67] where the Ti atom is at position ($\frac{3}{4}$, $\frac{1}{2}$) above atom #8. Figure 2.27 shows the results of the

calculations using the Vienna Ab-initio Simulation Package (VASP).[68–80] All three structures differ in total energy by only $0.1 - 0.2\,\mathrm{eV}$, meaning that all three structures could theoretically form. Another visible aspect is the strong difference in activation energy for the formation of the two different (2×1) structures. The structure proposed in this work has with $1.2\,\mathrm{eV}$ coming from the unreconstructed surface the smaller energy barrier compared to the $1.6\,\mathrm{eV}$ necessary for the $SrTiO_3$-(2×1) structure. This confirms the stability of the proposed structure and explains the preference of $BaTiO_3$ to reconstruct this way as opposed to $SrTiO_3$ as reported by Herger *et al.*[66, 67]
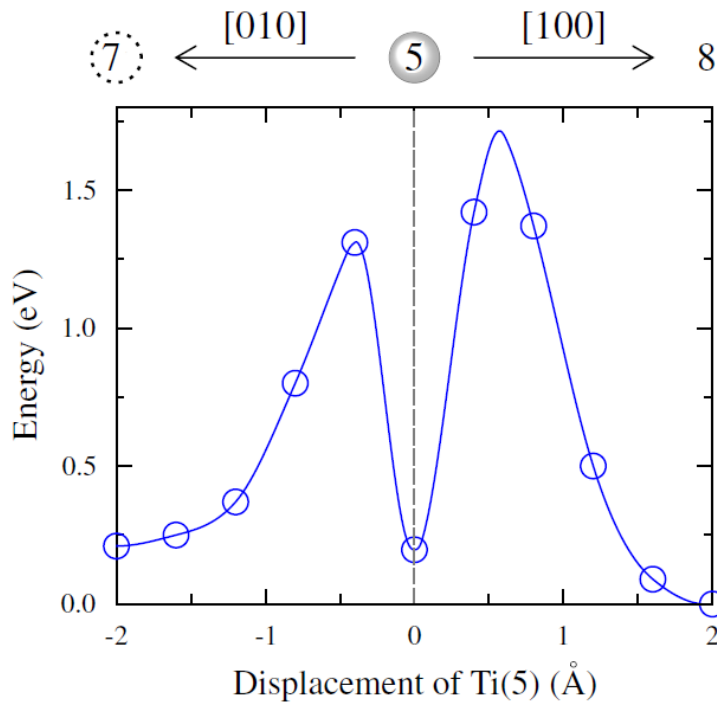
Figure 2.27: Calculated total energy versus Titanium atom displacement. Labels (7), (5), and (8) correspond to the Ti position for the BTO-(1×1), BTO-p(2×1) and the STO-p(2×1) structure, respectively. The numbers also correspond to the atom numbers in Figures 2.25 and 2.26(b) denoting the in-plane position of the displaced Titanium atom.[43]

In addition to structural stability, electronic and magnetic properties were investigated by density functional theory calculations using a Korringa-Kohn-Rostoker Green-function method. The spin-resolved Density of States (DOS) of a TiO_2 terminated $BaTiO_3(001)$-$(1×1)$ surface is compared to the $BaTiO_3(001)$-p(2×1) surface in Figure 2.28. The $BaTiO_3(001)$-(1×1) DOS in the top part of this Figure is based on the calculations by Fechner *et al.*[7] and shows a

quasimetallic behavior. Here hybridized Ti $3d$ and O $2p$ states form the band structure at and below the Fermi level and antibonding Ti $3d$ states are situated about $3 - 5\,\text{eV}$ above the Fermi level. One can see similar distribution of the DOS for Titanium and Oxygen leading to the conclusion, that the Ti $3d$ and O $2p$ states' hybridization is very strong. The quasimetallic DOS does not correspond to the insulating behavior of $BaTiO_3$ but it might easily be destroyed by imperfections always present in the non-ideal crystal.
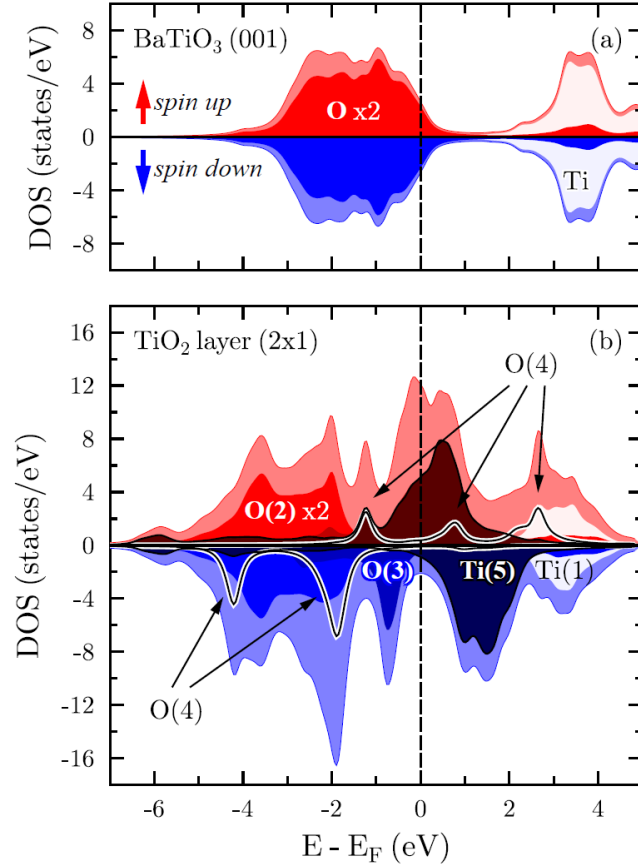
Figure 2.28: Spin resolved Density of States calculations for the (1×1) (top) and p(2×1) reconstructed $BaTiO_3(001)$ where the atom numbers in parentheses correspond to the scheme used in Figure 2.25.[43]

For the p(2×1) reconstructed $BaTiO_3$ the Density of States in the bottom part of Figure 2.28 shows a quite different behavior. It shows strong metallicity resulting from the Titanium atom #5 hybridizing with the surrounding Oxygen atoms. Titanium atom #5 shows a strong shift of the antibonding $3d$ states towards the Fermi level which matches a charge transfer towards the Titanium. This coincides with the partially unoccupied $2p$ states visible for Oxygen #4.

These magnetic moments were calculated and are included in the spin density contour plot of Figure 2.29. Shown is a cut along the [100] and [001] directions through the spin density map calculated for the Titanium and Oxygen atoms of the TiO_2 double layer in the $BaTiO_3(001)$-p(2×1) reconstructed surface. The Titanium #5 and Oxygen #4 have large magnetic moments of $+1.3\,\mu_B$ and $-2.0\,\mu_B$, respectively, which are antiferromagnetically coupled with a strongly localized interaction. Oxygen #3 behaves differently in such a way, that it forms a magnetic chain along the [010] direction with $-0.5\,\mu_B$ local magnetic moment. This leads to the surface magnetic structure being composed of parallel magnetic chains at a distance of approximately $8\,\text{Å}$ from each other and centered in the space between the chains a localized magnetic structure appears every $4\,\text{Å}$.
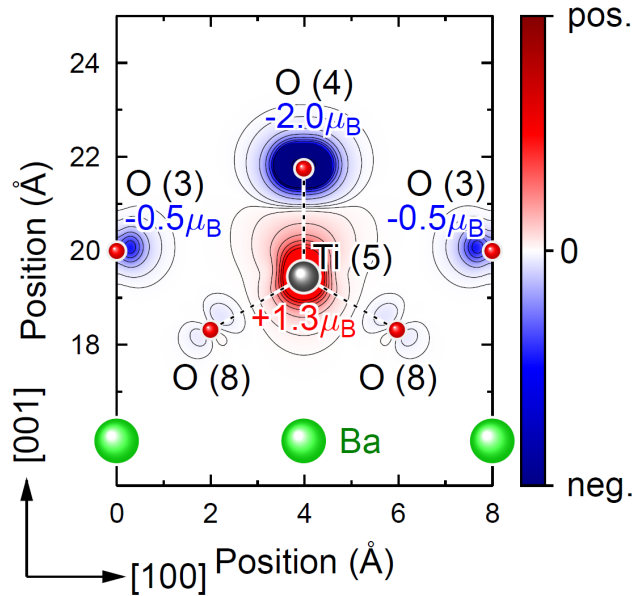
Figure 2.29: Calculations for the $BaTiO_3(001)$-p(2×1) surface showing the spin density and magnetic moments of the Titanium and Oxygen atoms.[43]

This shows, that the (2×1) reconstruction of $BaTiO_3(001)$ leads to a metallic character and an intrinsic magnetic structure of the surface. Santander-Syro *et al.*[81] investigated the metallic character of the $SrTiO_3$ surface which is largely independent of the bulk doping level. If their metallicity can be explained by this surface model it would support the claim, that this metallic character is a property of all perovskite surfaces.

Chapter 3

Summary

In this work the preparation and geometric structure of Barium Titanate films grown by Pulsed Laser Deposition were experimentally investigated by Surface X-Ray Diffraction and supported by theoretical calculations. The influence of lattice mismatch in the range of -1.5% to 2.6% and different film thicknesses up to 3 unit cells was studied. Theoretical calculations involving the magnetic properties of the $BaTiO_3/Fe(001)$ system confirmed magnetic coupling between the Iron surface and the Titanium atoms. Additionally a new structural model for the $BaTiO_3(001)$-(2×1) reconstruction has been developed on the basis of SXRD measurements.

The growth of all $BaTiO_3$ films of this experiment proved to be Stranski-Krastanov like with a TiO_2 interfacial layer and a $c(2 \times 2)$ reconstruction. During growth of $BaTiO_3$ on $Pd(001)$ and $Pt(001)$ distinct amounts of Oxygen were incorporated into the interface and $BaTiO_3$ grew contrary to the $BaTiO_3/Fe(001)$ system not in complete unit cell layers throughout the whole film. This is due to the fact, that the adsorption of Oxygen into the interface leads to a charge neutralization of the TiO_2-$MetalO_x$ stack and the charge neutral growth of $BaTiO_3$ as complete unit cell layers does not start with the interfacial TiO_2 but with the succeeding BaO layer. Thus the $BaTiO_3$ film terminates with TiO_2 and not with BaO. For the $Pd(001)$ sample, due to the lower amount of Oxygen, this leads to a mixed termination since parts of the substrate-film interface has no additional Oxygen. The $Pt(001)$ sample is fully terminated by TiO_2.

All samples showed spontaneous polarization of the Barium Titanate in

the form of vertical shift between the Titanium and Oxygen atoms, except the sample with only one unit cell of coverage which proves an onset of spontaneous polarization of $BaTiO_3$ between one and two unit cells thickness. This onset might be related to the bulklike coordination of the TiO_2 layer starting with two unit cells. The calculations for Figure 1.3 accurately predicted the change in vertical shift inside the TiO_2 layers. Substrates with larger in-plane lattice constants lead to larger out-of-plane constants and a larger deviation in length between the longer and shorter TiO bond. Vertical shift in the termination layer provides a flat isocharge surface in order to achieve a charge neutral termination.

Connected to the polarization is the magnetic coupling calculated for the Iron sample. The position of the interfacial Titanium atom normal to the surface determines the orbital overlap with Iron and influences the magnetic moment of the Titanium changing from $0.03\mu_B$ ($P_\uparrow$) to $-0.35\mu_B$ ($P_\downarrow$) corresponding to ferromagnetic and antiferromagnetic coupling via the interface, respectively. Both of these states have been calculated and seem to be energetically stable in theory but only the ferromagnetic coupling has, as of yet, been measured experimentally.

Ordered growth of Fe on top of $BaTiO_3$ has not been achieved in this work but based on the theory that the free surface energies prevent the ordered growth, further experiments with Oxygen assisted deposition might prove successful.

The investigation of the clean $BaTiO_3(001)$ crystal in its $p(2 \times 1)$ reconstruction shows the distinct feature of a Titanium atom inside a tetragonal pyramid of Oxygen. This feature leads to a strong metallicity of the surface and a strong magnetic signal of $+1.3\mu_B$ and $-2.0\mu_B$ for the Titanium and the pyramid tip Oxygen, respectively. This model might also explain the recently investigated metallic character of the $SrTiO_3$ surface[81] or even prove to be a property of all perovskite oxide surfaces.

Future work should focus on directly influencing the polarization and creating practical switching behavior if possible. Further experiments should be performed to realize a Metal/$BaTiO_3$/Metal structure in order to practically realize the structure investigated by Duan *et al.*[5] Especially interesting is the reasoning by Meyerheim *et al.* and Tusche *et al.* for the Fe/MgO/Fe(001)

system.[51–54]

66

Bibliography

[1]   J. F. Scott. „Data storage: Multiferroic memories". In: *Nature Materials* 6.4 (2007), pp. 256–257. ISSN: 1476-1122.

[2]   Martin Gajek, Manuel Bibes, Stephane Fusil, Karim Bouzehouane, Josep Fontcuberta, Agnes Barthelemy, and Albert Fert. „Tunnel junctions with multiferroic barriers". In: *Nature Materials* 6.4 (2007), pp. 296–302. ISSN: 1476-1122. DOI: `10.1038/nmat1860`.

[3]   Thomas Lottermoser, Thomas Lonkai, Uwe Amann, Dietmar Hohlwein, Jorg Ihringer, and Manfred Fiebig. „Magnetic phase control by an electric field". In: *Nature* 430.6999 (2004), pp. 541–544. ISSN: 0028-0836. DOI: `10.1038/nature02728`.

[4]   Nicola A. Hill. „Why Are There so Few Magnetic Ferroelectrics?" In: *The Journal of Physical Chemistry B* 104.29 (2000), pp. 6694–6709. DOI: `10.1021/jp000114x`.

[5]   Chun-Gang Duan, S. S. Jaswal, and E. Y. Tsymbal. „Predicted Magnetoelectric Effect in $Fe/BaTiO_3$ Multilayers: Ferroelectric Control of Magnetism". In: *Physical Review Letters* 97.4, 047201 (2006), p. 047201. DOI: `10.1103/PhysRevLett.97.047201`.

[6]   Evgeny Y. Tsymbal and Hermann Kohlstedt. „Tunneling Across a Ferroelectric". In: *Science* 313.5784 (2006), pp. 181–183. DOI: `10.1126/science.1126230`.

[7]   M. Fechner, S. Ostanin, and I. Mertig. „Effect of the surface polarization in polar perovskites studied from first principles". In: *Physical Review B: Condensed Matter and Materials Physics* 77.9, 094112 (2008), p. 094112. DOI: `10.1103/PhysRevB.77.094112`.

[8]   Julian P. Velev, Chun-Gang Duan, Kirill D. Belashchenko, Sitaram S. Jaswal, and Evgeny Y. Tsymbal. „Effects of ferroelectricity and magnetism on electron and spin transport in $Fe/BaTiO_3/Fe$ multiferroic tunnel junctions". In: *Journal of Applied Physics* 103.7, 07A701 (2008), 07A701. DOI: 10.1063/1.2828512.

[9]   V. Garcia, M. Bibes, L. Bocher, S. Valencia, F. Kronast, A. Crassous, X. Moya, S. Enouz-Vedrenne, A. Gloter, D. Imhoff, C. Deranlot, N. D. Mathur, S. Fusil, K. Bouzehouane, and A. Barthélémy. „Ferroelectric Control of Spin Polarization". In: *Science* 327.5969 (2010), pp. 1106–1110. DOI: 10.1126/science.1184028.

[10]   Hans Lüth. *Solid Surfaces, Interfaces and Thin Films*. Springer Berlin Heidelberg, 2010. DOI: 10.1007/978-3-642-13592-7.

[11]   David P. Norton. „Pulsed Laser Deposition of Complex Materials: Progress Toward Applications. applications-led growth of functional materials". In: *Pulsed Laser Deposition of Thin Films*. Ed. by Robert Eason. Wiley-Interscience, 2007. Chap. 1, pp. 1–32. ISBN: 978-0-471-44709-2.

[12]   Gerd Binnig and Heinrich Rohrer. „Scanning tunneling microscopy—from birth to adolescence". In: *Reviews of Modern Physics* 59.3 (1987), pp. 615–625. DOI: 10.1103/RevModPhys.59.615.

[13]   R. Feidenhans'l. „Surface structure determination by X-ray diffraction". In: *Surface Science Reports* 10.3 (1989), pp. 105 –188. ISSN: 0167-5729. DOI: 10.1016/0167-5729(89)90002-2.

[14]   I. K. Robinson. „Crystal truncation rods and surface roughness". In: *Physical Review B: Condensed Matter and Materials Physics* 33.6 (1986), pp. 3830–3836. DOI: 10.1103/PhysRevB.33.3830.

[15]   I. K. Robinson. „Surface Crystallography". In: *Handbook on Synchroton Radiation*. Ed. by G. Brown and D. E. Moncton. Vol. 3. Elsevier Science Publishers B.V., 1991. Chap. Surface Crystallography, pp. 221–266.

[16]   M. Adachi, Y. Akishige, T. Asahi, K. Deguchi, K. Gesi, K. Hasebe, T. Hikita, T. Ikeda, Y. Iwata, M. Komukae, T. Mitsui, E. Nakamura, N. Nakatani, M. Okuyama, T. Osaka, A. Sakai, E. Sawaguchi, Y. Shiozaki, T. Takenaka, K. Toyoda, T. Tsukamoto, and T. Yagi. „Landolt-Börnstein

- Group III Condensed Matter". In: vol. 36A1. Landolt-Börnstein. Springer-Verlag, 2002. Chap. Simple perowskite-type oxides - Titanates. DOI: 10.1007/b53034.

[17] Millicent B. Smith, Katharine Page, Theo Siegrist, Peter L. Redmond, Erich C. Walter, Ram Seshadri, Louis E. Brus, and Michael L. Steigerwald. „Crystal Structure and the Paraelectric-to-Ferroelectric Phase Transition of Nanoscale BaTiO3". In: *Journal of the American Chemical Society* 130.22 (2008), pp. 6955–6963. DOI: 10.1021/ja0758436.

[18] Eugene Heifets, Simon Dorfman, David Fuks, and Eugene Kotomin. „Atomistic simulation of the [001]surface structure in BaTiO3". In: *Thin Solid Films* 296.1-2 (1997). European Materials Research Society 1996 Spring Meeting, Symposium B: Thin Film Materials for Large Area Electronics, pp. 76 –78. ISSN: 0040-6090. DOI: 10.1016/S0040-6090(96)09348-0.

[19] Tatsuo Schimizu and Takashi Kawakubo. „First-Principles Approach to the Effect of c-axis Elongation of BaTiO$_3$ Thin Films". In: *Japanese Journal of Applied Physics* 37.Part 2, No. 2B (1998), pp. L235–L237. DOI: 10.1143/JJAP.37.L235.

[20] Hiromu Miyazawa, Eiji Natori, Tatsuya Shimoda, Hiroki Kishimoto, Fumiyuki Ishii, and Tamio Oguchi. „Relationship between Lattice Deformation and Polarization in BaTiO$_3$". In: *Japanese Journal of Applied Physics* 40.Part 1, No. 9B (2001), pp. 5809–5811. DOI: 10.1143/JJAP.40.5809.

[21] A. Ernst. *Personal communication.* 2011.

[22] H. L. Meyerheim and J. Kirschner. „Wachstum, Struktur und magnetische Eigenschaften ultradünner Übergangsmetalloxide auf Metallen". In: *SFB 762 Funktionalität Oxidischer Grenzflächen. September 14.-15.2011, Halle (Poster).*

[23] Howard M. Smith and A. F. Turner. „Vacuum Deposited Thin Films Using a Ruby Laser". In: *Applied Optics* 4.1 (1965), pp. 147–148. DOI: 10.1364/AO.4.000147.

[24]   K. R. Chen, J. N. Leboeuf, R. F. Wood, D. B. Geohegan, J. M. Donato, C. L. Liu, and A. A. Puretzky. „Mechanisms affecting kinetic energies of laser-ablated materials". In: *Journal of Vacuum Science & Technology A: Vacuum, Surfaces, and Films* 14.3 (1996), pp. 1111–1114. ISSN: 07342101. DOI: 10.1116/1.580278.

[25]   Omicron NanoTechnology GmbH. *EFM3 - Omicron NanoTechnology GmbH*. Ed. by Andreas Frank. 2011. URL: http://www.omicron.de/en/products/efm-3-/instrument-concept.

[26]   J. Kirschner, H. Engelhard, and D. Hartung. „An evaporation source for ion beam assisted deposition in ultrahigh vacuum". In: *Review of Scientific Instruments* 73.11 (2002), pp. 3853–3860. ISSN: 00346748. DOI: 10.1063/1.1511791.

[27]   Saes Getters S.p.A. *Barium Getter Features*. Ed. by Saes Getters S.p.A. 2011. URL: http://www.saesgetters.com/default.aspx?idPage=460.

[28]   Kenton D. Childs. *Handbook of Auger electron spectroscopy: a reference book of standard data for identification and interpretation of Auger electron spectroscopy data*. 3rd ed. Physical Electronics Industries, 1995, p. 405. ISBN: 0-9648124-0-1.

[29]   Dirk Ullmann. „Herstellung und Charakterisierung epitaktischer Fe(001)/ MgO/Fe - Tunnelmagnetowiderstände". Dissertation. Martin-Luther- Universität Halle-Wittenberg, 2002.

[30]   K.W. Hipps. „Scanning Tunneling Spectroscopy (STS)". In: *Handbook of Applied Solid State Spectroscopy*. Ed. by D. R. Vij. 2006.

[31]   C. Julian Chen. *Introduction to Scanning Tunneling Microscopy (Oxford Series in Optical & Imaging Sciences)*. Oxford University Press, USA, 1993. ISBN: 0195071506.

[32]   I. Horcas, R. Fernández, J. M. Gómez-Rodríguez, J. Colchero, J. Gómez-Herrero, and A. M. Baro. „WSXM: A software for scanning probe microscopy and a tool for nanotechnology". In: *Review of Scientific Instruments* 78.1, 013705 (2007), p. 013705. DOI: 10.1063/1.2432410.

[33] M. Born and E. Wolf. *Principles of optics: electromagnetic theory of propagation, interference and diffraction of light*. Pergamon Press, 1975. ISBN: 9780080139876.

[34] P. Kraft, A. Bergamaschi, Ch. Brönnimann, R. Dinapoli, E. F. Eikenberry, B. Henrich, I. Johnson, A. Mozzanica, C. M. Schlepütz, P. R. Willmott, and B. Schmitt. „Performance of single-photon-counting PILATUS detector modules". In: *Journal of Synchrotron Radiation* 16.3 (2009), pp. 368–375. DOI: `10.1107/S0909049509009911`.

[35] C. M. Schlepütz, R. Herger, P. R. Willmott, B. D. Patterson, O. Bunk, Ch. Brönnimann, B. Henrich, G. Hülsen, and E. F. Eikenberry. „Improved data acquisition in grazing-incidence X-ray scattering experiments using a pixel detector". In: *Acta Crystallographica Section A* 61.4 (2005), pp. 418–425. DOI: `10.1107/S0108767305014790`.

[36] B. A. Sobott, C. Brönnimann, E. F. Eikenberry, R. Dinapoli, P. Kraft, G. N. Taylor, P. R. Willmott, C. M. Schlepütz, and R. P. Rassool. „Synchrotron radiation hardness studies of PILATUS II". In: *Journal of Synchrotron Radiation* 16.4 (2009), pp. 489–493. DOI: `10.1107/S0909049509014733`.

[37] MATLAB. *version 7.11.0 (R2010b)*. Natick, MA, USA: The MathWorks Inc., 2010.

[38] Christian M. Schlepütz. „Systematic Structure Investigation of YBCO Thin Films with Direct Methods and Surface X-ray Diffraction". Dissertation. Universität Zürich, 2009.

[39] C. Schamper, H. L. Meyerheim, and W. Moritz. „Resolution correction for surface X-ray diffraction at high beam exit angles". In: *Journal of Applied Crystallography* 26.5 (1993), pp. 687–696. DOI: `10.1107/S0021889893004364`.

[40] U. H. Zucker, E. Perenthaler, W. F. Kuhs, R. Bachmann, and H. Schulz. „*PROMETHEUS*. A program system for investigation of anharmonic thermal vibrations in crystals". In: *Journal of Applied Crystallography* 16.3 (1983), p. 358. DOI: `10.1107/S0021889883010560`.

[41]   S. C. Abrahams. „Indicators of accuracy in structure factor measurement". In: *Acta Crystallographica Section A* 25.1 (1969), pp. 165–173. DOI: 10.1107/S0567739469000283.

[42]   A. L. Patterson. „A Fourier Series Method for the Determination of the Components of Interatomic Distances in Crystals". In: *Physical Review* 46.5 (1934), pp. 372–376. DOI: 10.1103/PhysRev.46.372.

[43]   H. L. Meyerheim, A. Ernst, K. Mohseni, I. V. Maznichenko, S. Ostanin, F. Klimenta, N. Jedrecy, W. Feng, I. Mertig, R. Felici, and J. Kirschner. „BaTiO$_3$(001)-(2×1): Surface Structure and Spin Density". In: *Physical Review Letters* 108 (21 2012), p. 215502. DOI: 10.1103/PhysRevLett.108.215502.

[44]   Th. Hahn. „International Tables for Crystallography Volume A: Space-group symmetry". In: ed. by Th. Hahn. Fifth edition. Vol. A. Springer Netherlands, 2002. Chap. The 17 plane groups (two-dimensional space groups), pp. 91–109. DOI: 10.1107/97809553602060000512.

[45]   J. Kirschner. „Polarized electron diffraction from clean and adsorbate covered Fe(110)". In: *Surface Science* 138.1 (1984), pp. 191 –202. ISSN: 0039-6028. DOI: DOI:10.1016/0039-6028(84)90505-3.

[46]   J. I. Langford and A. J. C. Wilson. „Scherrer after sixty years: A survey and some new results in the determination of crystallite size". In: *Journal of Applied Crystallography* 11.2 (1978), pp. 102–113. DOI: 10.1107/S0021889878012844.

[47]   H. L. Meyerheim, F. Klimenta, A. Ernst, K. Mohseni, S. Ostanin, M. Fechner, S. Parihar, I. V. Maznichenko, I. Mertig, and J. Kirschner. „Structural Secrets of Multiferroic Interfaces". In: *Physical Review Letters* 106.8 (2011), p. 087203. DOI: 10.1103/PhysRevLett.106.087203.

[48]   M. Fechner, I. V. Maznichenko, S. Ostanin, A. Ernst, J. Henk, P. Bruno, and I. Mertig. „Magnetic phase transition in two-phase multiferroics predicted from first principles". In: *Physical Review B: Condensed Matter and Materials Physics* 78.21, 212406 (2008), p. 212406. DOI: 10.1103/PhysRevB.78.212406.

[49] Chun-Gang Duan, Renat F. Sabirianov, Wai-Ning Mei, Sitaram S. Jaswal, and Evgeny Y. Tsymbal. „Interface Effect on Ferroelectricity at the Nanoscale". In: *Nano Letters* 6.3 (2006), pp. 483–487. DOI: `10.1021/nl0524521`.

[50] A. Ernst. *Personal communication.* 2012.

[51] H. L. Meyerheim, R. Popescu, J. Kirschner, N. Jedrecy, M. Sauvage-Simkin, B. Heinrich, and R. Pinchaux. „Geometrical and Compositional Structure at Metal-Oxide Interfaces: MgO on Fe(001)". In: *Physical Review Letters* 87.7 (2001), p. 076102. DOI: `10.1103/PhysRevLett.87.076102`.

[52] H. L. Meyerheim, R. Popescu, N. Jedrecy, M. Vedpathak, M. Sauvage-Simkin, R. Pinchaux, B. Heinrich, and J. Kirschner. „Surface x-ray diffraction analysis of the MgO/Fe(001) interface: Evidence for an FeO layer". In: *Physical Review B: Condensed Matter and Materials Physics* 65.14 (2002), p. 144433. DOI: `10.1103/PhysRevB.65.144433`.

[53] C. Tusche, H. L. Meyerheim, N. Jedrecy, G. Renaud, A. Ernst, J. Henk, P. Bruno, and J. Kirschner. „Oxygen-Induced Symmetrization and Structural Coherency in $Fe/MgO/Fe$(001) Magnetic Tunnel Junctions". In: *Physical Review Letters* 95.17 (2005), p. 176101. DOI: `10.1103/PhysRevLett.95.176101`.

[54] C. Tusche, H. L. Meyerheim, N. Jedrecy, G. Renaud, and J. Kirschner. „Growth sequence and interface formation in the Fe/MgO/Fe(001) tunnel junction analyzed by surface x-ray diffraction". In: *Physical Review B: Condensed Matter and Materials Physics* 74.19, 195422 (2006), p. 195422. DOI: `10.1103/PhysRevB.74.195422`.

[55] L. Z. Mezey and J. Giber. „The Surface Free Energies of Solid Chemical Elements: Calculation from Internal Free Enthalpies of Atomization". In: *Japanese Journal of Applied Physics* 21.Part 1, No. 11 (1982), pp. 1569–1571. DOI: `10.1143/JJAP.21.1569`.

[56] S. H. Overbury, P. A. Bertrand, and G. A. Somorjai. „Surface composition of binary systems. Prediction of surface phase diagrams of solid solutions". In: *Chemical Reviews* 75.5 (1975), pp. 547–560. ISSN: 0009-2665. DOI: `10.1021/cr60297a001`.

[57] R. I. Eglitis and David Vanderbilt. „Ab initio calculations of BaTiO$_3$ and PbTiO$_3$ (001) and (011) surface structures". In: *Physical Review B: Condensed Matter and Materials Physics* 76.15, 155439 (2007), p. 155439. DOI: `10.1103/PhysRevB.76.155439`.

[58] R. Courths. „Ultraviolet Photoelectron Spectroscopy (UPS) and LEED Studies of BaTiO$_3$ (001) and SrTiO$_3$ (100) Surfaces". In: *Physica Status Solidi B: Basic Solid State Physics* 100.1 (1980), pp. 135–148. DOI: `10.1002/pssb.2221000114`.

[59] Daniel Aberdam, Gérard Bouchet, and Pierre Ducros. „LEED study of surface structures on the (001) face of BaTiO$_3$". In: *Surface Science* 27.3 (1971), pp. 559 –570. ISSN: 0039-6028. DOI: `10.1016/0039-6028(71)90188-9`.

[60] Tetsushi Shimizu, Hiroshi Bando, Yoshihiro Aiura, Yuichi Haruyama, Kunihiko Oka, and Yoshikazu Nishihara. „Scanning Tunneling Microscopy and Spectroscopy Observation of Reduced BaTiO$_3$(100) Surface". In: *Japanese Journal of Applied Physics* 34.Part 2, No. 10A (1995), pp. L1305–L1308. DOI: `10.1143/JJAP.34.L1305`.

[61] Hiroshi Bando, Tetsushi Shimitzu, Yoshihiro Aiura, Yuichi Haruyama, Kunihiko Oka, and Yoshikazu Nishihara. „Structure and electronic states on reduced BaTiO$_3$ (100) surface observed by scanning tunneling microscopy and spectroscopy". In: *Journal of Vacuum Science & Technology B: Microelectronics and Nanometer Structures* 14.2 (1996), pp. 1060–1063. DOI: `10.1116/1.588400`.

[62] Christian Hagendorf. „Oberflächenphysikalische Untersuchungen an ein- und polykristallinem BaTiO$_3$". Dissertation. Martin-Luther-Universität Halle-Wittenberg, 2000.

[63] Alexie M. Kolpak, Dongbo Li, Rui Shao, Andrew M. Rappe, and Dawn A. Bonnell. „Evolution of the Structure and Thermodynamic Stability of the *BaTiO$_3$*(001) Surface". In: *Physical Review Letters* 101.3 (2008), p. 036102. DOI: `10.1103/PhysRevLett.101.036102`.

[64] N Iles, F Finocchi, and K Driss Khodja. „A systematic study of ideal and double layer reconstructions of ABO 3 (001) surfaces (A = Sr, Ba; B =

Ti, Zr) from first principles". In: *Journal of Physics: Condensed Matter* 22.30 (2010), p. 305001. DOI: `10.1088/0953-8984/22/30/305001`.

[65] Natasha Erdman, Kenneth R. Poeppelmeier, Mark Asta, Oliver Warschkow, Donald E. Ellis, and Laurence D. Marks. „The structure and chemistry of the TiO2-rich surface of SrTiO3 (001)". In: *Nature* 419.6902 (2002), pp. 55–58. ISSN: 0028-0836. DOI: `10.1038/nature01010`.

[66] R. Herger, P. R. Willmott, O. Bunk, C. M. Schlepütz, B. D. Patterson, B. Delley, V. L. Shneerson, P. F. Lyman, and D. K. Saldin. „Surface structure of $SrTiO_3$ (001)". In: *Physical Review B: Condensed Matter and Materials Physics* 76.19 (2007), p. 195435. DOI: `10.1103/PhysRevB.76.195435`.

[67] R. Herger, P. R. Willmott, O. Bunk, C. M. Schlepütz, B. D. Patterson, and B. Delley. „Surface of Strontium Titanate". In: *Physical Review Letters* 98.7, 076102 (2007), p. 076102. DOI: `10.1103/PhysRevLett.98.076102`.

[68] P. E. Blöchl. „Projector augmented-wave method". In: *Physical Review B: Condensed Matter and Materials Physics* 50.24 (1994), pp. 17953–17979. DOI: `10.1103/PhysRevB.50.17953`.

[69] G. Kresse and J. Furthmüller. „Efficiency of ab-initio total energy calculations for metals and semiconductors using a plane-wave basis set". In: *Computational Materials Science* 6 (1996), p. 15.

[70] G. Kresse and J. Furthmüller. „Efficient iterative schemes for ab initio total-energy calculations using a plane-wave basis set". In: *Physical Review B: Condensed Matter and Materials Physics* 54.16 (1996), pp. 11169–11186. DOI: `10.1103/PhysRevB.54.11169`.

[71] G. Kresse and J. Hafner. „Ab initio molecular-dynamics simulation of the liquid-metal-amorphous-semiconductor transition in germanium". In: *Physical Review B: Condensed Matter and Materials Physics* 49 (1994), p. 14251.

[72] G. Kresse and J. Hafner. „Norm-Conserving and Ultrasoft Pseudopotentials for First-Row and Transition-Elements". In: *Journal of Physics: Condensed Matter* 6 (1994), p. 8245.

[73]   G. Kresse and J. Hafner. „Ab initio molecular dynamics for liquid met-
       als“. In: *Physical Review B: Condensed Matter and Materials Physics* 47
       (1993), p. 558.

[74]   G. Kresse and D. Joubert. „From ultrasoft pseudopotentials to the pro-
       jector augmented-wave method“. In: *Physical Review B: Condensed Mat-
       ter and Materials Physics* 59 (1999), p. 1758.

[75]   J.P. Perdew, J.A. Chevary, S.H. Vosko, K.A. Jackson, M.R. Pederson,
       D.J. Singh, and C. Fiolhais. „Erratum: Atoms, Molecules, Solids, and
       Surfaces: Applications of the Generalized Gradient Approximation for
       Exchange and Correlation“. In: *Physical Review B: Condensed Matter
       and Materials Physics* 48 (1993), p. 4978.

[76]   J.P. Perdew, J.A. Chevary, S.H. Vosko, K.A. Jackson, M.R. Pederson,
       D.J. Singh, and C. Fiolhais. „Atoms, Molecules, Solids, and Surfaces: Ap-
       plications of the Generalized Gradient Approximation for Exchange and
       Correlation“. In: *Physical Review B: Condensed Matter and Materials
       Physics* 46 (1992), p. 6671.

[77]   J. P. Perdew, K. Burke, and M. Ernzerhof. „Erratum: Generalized Gradi-
       ent Approximation Made Simple“. In: *Physical Review Letters* 78 (1997),
       p. 1396.

[78]   J. P. Perdew, K. Burke, and M. Ernzerhof. „Generalized Gradient Ap-
       proximation Made Simple“. In: *Physical Review Letters* 77 (1996), p. 3865.

[79]   J. P. Perdew and A. Zunger. „Self-Interaction Correction to Density-
       Functional Approximations for Many-Electron Systems“. In: *Physical Re-
       view B: Condensed Matter and Materials Physics* 23 (1981), p. 5048.

[80]   D. Vanderbilt. „Soft Self-Consistent Pseudopotentials in a Generalized
       Eigenvalue Formalism“. In: *Physical Review B: Condensed Matter and
       Materials Physics* 41 (1990), p. 7892.

[81]   A. F. Santander-Syro, O. Copie, T. Kondo, F. Fortuna, S. Pailhes, R.
       Weht, X. G. Qiu, F. Bertran, A. Nicolaou, A. Taleb-Ibrahimi, P. Le
       Fevre, G. Herranz, M. Bibes, N. Reyren, Y. Apertet, P. Lecoeur, A.
       Barthelemy, and M. J. Rozenberg. „Two-dimensional electron gas with

universal subbands at the surface of SrTiO3". In: *Nature* 469.7329 (2011), pp. 189–193. ISSN: 0028-0836.

Curriculum Vitae

Persönliche Information

Name, Vorname:	KLIMENTA, Florian
Geburtsdatum, -ort:	17. Dezember 1982, Halberstadt, Deutschland
Staatsbürgerschaft:	Deutsch

Ausbildung

1989-1993	Grundschule "Thomas Mann" Dardesheim
1993-2002	Fallstein-Gymnasium Osterwieck
1999-2000	Austauschjahr: Bonner Springs High School, Bonner Springs, KS, USA
2002	Abitur
2002-2003	Wehrdienst Veitshöchheim
2003-2009	Diplomstudium Physik, Technische Universität Chemnitz
2009	Diplomarbeit "CoPt auf periodischen Nanostrukturen"
2009-2012	Promotionsstudium, Max-Planck-Institut für Mikrostrukturphysik, Halle und Martin-Luther-Universität Halle-Wittenberg
2012	Dissertation "Preparation, geometric structure and magnetism of ultrathin oxide films on metal surfaces"

Selbständigkeitserklärung

Ich erkläre, dass ich keine andere als die von mir angegebenen Quellen und Hilsmittel zur Erstellung meiner Dissertation verwendet habe. Den benutzten Werken wörtlich oder inhaltlich entnommene Stellen sind als solche gekennzeichnet.

Florian Klimenta

Halle (Saale), 28.09.2012